Inhomogeneous hard platelet fluids

Inaugural-Dissertation
zur
Erlangung des Doktorgrades der
Mathematisch-Naturwissenschaftlichen Fakultät
der Heinrich-Heine Universität Düsseldorf

vorgelegt von

THORSTEN HENDRIK BOZZO REICH

aus Düsseldorf

Düsseldorf, Dezember 2006

Aus dem Institut für Theoretische Physik II
der Heinrich-Heine Universität Düsseldorf

Gedruckt mit Genehmigung der
Mathematisch-Naturwissenschaftlichen Fakultät der
Heinrich-Heine Universität Düsseldorf

Referent:	Prof. Dr. H. Löwen
Koreferent:	PD Dr. Matthias Schmidt

Tag der mündlichen Prüfung: 19. Januar 2007

This thesis bases on the following papers:

Chapter 2 (theory):
A. Esztermann, H. Reich, M. Schmidt
Density functional theory for colloidal mixtures of hard platelets, rods and spheres,
PRE **73**, 011409 (2006)

Chapter 3:
H. Reich, M. Dijkstra, R. van Roij, M. Schmidt.
Entropic wetting and the free isotropic nematic interface of hard colloidal platelets,
to be published

A short account of chapter3 has been published in:
D. van der Beek, H. Reich, P. van der Schoot, M. Dijkstra, T. Schilling, R. Vink, M. Schmidt, R. van Roij, H.N.W. Lekkerkerker
Isotropic-nematic interface and wetting in suspensions of colloidal platelets,
PRL **97**, 087801 (2006)

Abstract

The focus of this thesis lies on the investigation of inhomogeneous fluids of (infinitely thin) hard platelets. For reasons of comparison, we also treat the system of (infinitely thin) hard rods in some chapters. The investigations are done by using Density Functional Theory (DFT). In particular, we use a recently developed Fundamental Measure Theory (FMT) functional that includes contributions to the free energy that are of third order in density.

In the first part, we address the bulk behaviour of hard platelets, their free isotropic-nematic interface as well as their behaviour in contact with a single planar hard wall. In our bulk calculations, we determine the bulk isotropic-nematic phase coexistence densities and calculate the equation of state in the isotropic and nematic phase. For both, we find good agreement with simulation results. Subsequently, we investigate the wetting behaviour of the platelets when adsorbed against a hard wall and find complete wetting. Surprisingly, our results show that oscillations of the isotropic wall profile disappear for increasing (bulk) densities.

The second part is about platelets in finite external fields. We first investigate the influence of a magnetic field on the location of the isotropic-nematic phase transition and find the transition to end in a critical point for strong magnetic fields. After considering the sedimentation of hard platelets under gravity, we study the sedimentation in the simultaneous presence of a magnetic field. We find that increasing magnetic field strength leads to lower densities at the bottom of the system.

In the third part, we investigate which effects occur in strong geometrical confinement, i.e. between two parallel hard walls and find a capillary critical point. For reasons of comparison, we perform these calculations also for rods between two parallel hard walls (acting on the centres of the rods) and find a smaller critical capillary width for the rods as compared to the platelets.

The last part of the thesis studies platelets and rods at finite thickness. We test a modification of the FMT functional and calculate the influence of the thickness of the particles on the isotropic-nematic phase transition. For platelets, we also calculate the equation of state. Our results are not satisfying for platelets nor for rods when compared to simulation results.

Zusammenfassung

Der Schwerpunkt dieser Doktorarbeit liegt auf der Untersuchung der Eigenschaften von inhomogenen Flüssigkeiten aus (unendlich dünnen) harten Plättchen. Aus Vergleichsgründen werden wir in einigen Kapiteln aber auch Flüssigkeiten aus (unendlich dünnen) harten Stäbchen betrachten. Die Untersuchungen wurden mit Hilfe der Dichtefunktionaltheorie (DFT) durchgeführt. Speziell wurde ein kürzlich entwickelter *Fundamental Measure Theory* (FMT) Ansatz verwendet, der Beiträge zur freien Energie enthält, die von dritter Ordnung in der Dichte sind.

Im ersten Teil der Arbeit untersuchen wir das Bulk-Verhalten von harten Plättchen, ihre freie isotrop-nematische Grenzfläche sowie das Verhalten der Plättchen beim Kontakt mit einer planen harten Wand. In unseren bulk-Rechnungen bestimmen wir die Koexistenz-Dichten am isotrop-nematischen Phasenübergang und berechnen die Zustandsgleichung in der isotropen und nematischen Phase. Für beide Punkte finden wir eine gute Übereinstimmung mit Simulations-Ergebnissen. Anschliessend untersuchen wir das Benetzungsverhalten der nematischen Phase der Plättchen beim Kontakt mit einer harten Wand und finden komplette Benetzung.

Im zweiten Teil beschäftigen wir uns mit Plättchen in endlichen externen Feldern. Wir untersuchen zunächst den Einfluss eines magnetischen Feldes auf den isotrop-nematischen Phasenübergang und finden, dass letzterer für ausreichend starke Felder in einem kritischen Punkt endet. Als nächstes widmen wir uns der Berechnung von Sedimentationsprofilen von harten Plättchen. Abschliessend studieren wir Sedimentation in einem gleichzeitig wirksamen magnetischen Feld. Wir beobachten eine Reduktion der Dichte am Boden des Systems für steigende magnetische Feldstärke.

Im dritten Teil untersuchen wir welche Effekte bei starkem geometrischen Einschluss, speziell zwischen zwei parallelen harten Wänden, auftreten und finden einen kritischen Wandabstand, bei dessen Unterschreitung kein isotrop-nematischer Übergang mehr auftritt. Aus Vergleichsgründen führen wir diese Rechnung auch für harte Stäbchen durch, wobei wir eine auf den Mittelpunkt der Stäbchen wirkende Wand annehmen. Es stellt sich heraus, dass der kritische Wandabstand für Stäbchen kleiner ist als für Plättchen.

Der letzte Teil der Doktorarbeit beschäftigt sich mit Plättchen und Stäbchen mit endlicher Dicke. Wir testen eine Modifikation des FMT-Funktionals und berechnen den Einfluss der Dicke auf den isotrop-nematischen Phasenübergang. Unsere Resultate zeigenin beiden Fällen keine zufriedenstellende Übereinstimmung mit Resultaten aus Simulationen.

Contents

Chapter 1

Introduction

Fluids we are exposed to in daily life, like e.g. water, consist of one or several components which are atoms or molecules. The size of the latter is in the order of magnitude of several Angstroms. The platelet fluid whose properties we investigate in this thesis is not such a molecular fluid, but belongs to the so-called *colloidal suspensions*. Colloidal suspensions are characterised by a molecular solvent (typical particle size $\approx 1\mathring{A}$), in which colloidal particles (typical size $\approx 10nm - 1\mu m$) are suspended. Due to this difference in size of about four orders of magnitude, the solvent can be treated as a continuum from the viewpoint of the colloids. This makes it possible to focus on the behaviour of the colloidal particles because the degrees of freedom of the solvent can be integrated out. Thus, when talking about fluids of *platelets*, one refers to the *suspended* component and not to the solvent.

Effects occurring in colloidal systems are for example the glass transition, interfacial phenomena or freezing and melting. Due to the fact that colloids belong to the mesoscopic time and length scale, such effects are much easier observable than in atomic systems. Hence, colloidal particles have become an important tool for studying these phenomena. One important phenomenon are phase transitions. The phase behaviour of colloidal suspensions is determined by the interactions between the particles. For charged colloids, Coulomb forces appear and cause nonlinear interactions with the counterions of the solvent. Thus, the peculiar features of these interactions are complicated and depend on the specific materials of which the colloids consist. However, due to the polarizability of the materials the colloids are (typically) made of, van der Waals interactions will appear. The van der Waals interaction, which is attractive, leads to a agglomeration of the colloidal particles. To avoid this, one can apply sterically or charge stabilisation. *Steric stabilisation* is reached by coating the colloids with polymer chains.

This leads to a repulsion between the colloids which is of entropic nature. *Charge stabilised* colloids interact by a screened Coulomb (Yukawa) interaction. Added salt ions contribute to the screening of the colloids and cause a short ranged interaction. Thus, both possibilities lead at last to interactions which can be modelled by the hard core pair potential, which is either zero (for non-overlapping pairs of particles) or infinite (for overlapping pairs of particles). Also this approximative model is not exactly solvable except in one dimension [1].

Beside the interactions, also the shape of the particles has an influence on the phase behaviour. Dispersions of nonspherical colloidal particles are model systems used to study a variety of phenomena in condensed matter, including fluid phase separation and liquid crystalline ordering. The possible shape of nonspherical objects is manifold and includes cut spheres, hexagons, spherodisks, platelets, rods etc., see [2] for a classification.

The phase behaviour of such nonspherical colloids is considerably more complex than that of spherical particles. The latter form a fluid phase at low densities and undergo a phase transition to a crystal upon increasing the density. In systems of nonspherical objects partially ordered phases with properties between those of the fluid and those of the crystal appear. One particularly important example is the phase transition from an isotropic (I) fluid to an orientationally ordered nematic (N) fluid. The IN transition was first observed experimentally in suspensions of (rod-like) tobacco mosaic virus particles [3, 4]. In Fig. 1.1 we plot a sketch of the isotropic, nematic and smectic phase of hard rods.

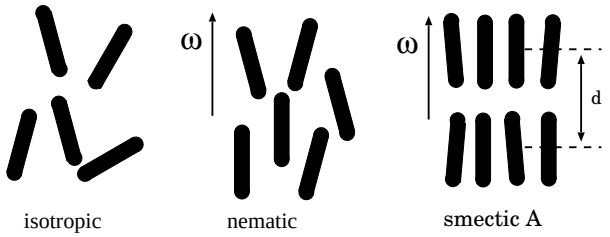

Figure 1.1: Sketch of the isotropic, nematic and smectic phase of hard rods. $\boldsymbol{\omega}$ denotes the nematic director. a) The *isotropic* phase is a totally disordered fluid phase. b) The *nematic* phase is characterised by an ordering of the orientations, while the centres of mass are still disordered. c) In the *smectic A* phase, the centres of mass are ordered in one spatial direction and disordered in the others; d is the spacing of the smectic layers.

The first theoretical description was given by Onsager [5]. This famous

treatment of macroscopic ordering due to anisotropic particle shapes constitutes a paradigm to understand the competition between position and orientation degrees of freedom that maximises the overall entropy of the system. Onsager's theory can be viewed as a truncation of the excess free energy functional at second order in density. It becomes exact, due to a scaling argument, in the limit of (vanishingly) thin rods at high concentration. However, such scaling does not hold in the case of (vanishingly) thin hard platelets; when applied to this system the theory is known to predict the bulk isotropic-nematic (IN) transition correctly to be of first order, but to overestimate the transition densities and value of the nematic order parameter at coexistence quite severely as compared to simulation results [6, 7]. The peculiar features of the bulk IN transition for platelets are its very small density jump at coexistence and its very low value of the nematic order parameter $S \approx 0.5$ in the coexisting nematic phase.

During the past several years considerable experimental, simulation and theoretical work has been devoted to platelet systems. A well established experimental model system are gibbsite platelets dispersed in toluene, for which the existence of the IN transition in a colloidal platelet system was for the first time observed with polarisation microscopy in Ref. [8]. For this system the nematic-columnar phase transition [9], the hexagonal-columnar liquid crystal phase [10], and gelation and nematic ordering [11] were investigated subsequently. Furthermore the influence of external potentials was considered, e.g. that of gravity [12, 13] and of electric [14] and magnetic [15] fields. Also platelike clay particles [16, 17] and mixtures of colloidal platelets and polymers [18,19] have received considerable attention. Theoretical investigations were devoted to the influence of gravity on phase behaviour [20], and the phenomenon of nematic density inversion [21]. The phase diagram of a mixture of hard colloidal spheres and disks was calculated using a free volume approach [22], and the free IN interface in fluids of charged platelike colloids was investigated using the Zwanzig model with discrete orientations [23]. Ref. [24] is devoted to the effects caused by polydispersity in a mixture of rods and platelets.

The presence of a substrate commonly leads to rich phenomenology of surface-induced phase behaviour. The smooth hard planar wall is a basic model for a substrate that despite its simplicity induces intriguing phenomena – and has accordingly attracted interest for a variety of hard core models: Examples include ordering of rods near a hard wall [25], the uniaxial-biaxial transition of hard rods [26–28], and wetting and layering transitions for model colloid-polymer mixtures [29–34]. The isotropic phase of platelets in contact with a wall has been considered in Ref. [35] using Onsager theory, and results

were compared to those for a hard rod fluid. For the Zwanzig model of platelets wetting and capillary effects were investigated [36] as well as bulk and interfacial properties of binary mixtures [37].

In this thesis we first consider vanishingly thin circular hard platelets with continuous orientations and address their bulk equation of state, the densities of the bulk isotropic-nematic (IN) coexistence, density profiles and the interface tension of the (planar) free IN interface, as well as their wetting properties when adsorbed against a planar hard wall. This is done in chapter 3. In chapter 4 we investigate platelets in magnetic and gravitational fields. Here we are interested in the influence of the magnetic field on the location of the IN transition as well as on sedimentation of platelets. Also the simultaneous presence of a magnetic and a gravitational field is considered. Chapter 5 follows with an investigation of effects which occur when platelets are exposed to strong geometrical confinement, i.e. between two planar hard walls. We compare our results for platelets with that for infinitely thin hard rods. We conclude in chapter 6 with platelets and rods with finite thickness.

For the platelets, we use a recently proposed fundamental measure theory (FMT) density functional [38] that includes contributions to the free energy that are of third order in density and predicts values of the coexistence densities and order parameter at the IN transition in good agreement with simulation results. The hard rods are treated with a FMT density functional which becomes exact in the Onsager limit of infinitely thin hard rods. We compare our results of chapter 2 obtained by FMT with that from Monte Carlo (MC) computer simulations, which were performed by M. Dijkstra from Utrecht University and with theoretical calculations for the Onsager limit, which were done by R. van Roij, also from Utrecht University. We thank both for the permission to use their results here.

Chapter 2

Model, theory and numerics

As the focus of this thesis lies on the investigation of infinitely thin hard platelets, we will introduce this system next. Then we give a short overview of the basics of classical density functional theory (DFT). After this we introduce Fundamental Measure Theory (FMT) and discuss briefly its application to hard platelets and hard rods. Finally, we describe the numerical procedure used.

2.1 Model

We consider a fluid of infinitely thin hard circular platelets of radius R. The platelets interact with a hard core pair potential $V(\mathbf{r}, \boldsymbol{\omega}, \boldsymbol{\omega}')$ that depends on the centre-to-centre distance $\mathbf{r}$ between both platelets and on both orientations, $\boldsymbol{\omega}$ and $\boldsymbol{\omega}'$, taken to be unit vectors perpendicular to the plane of the particle. $V(\mathbf{r}, \boldsymbol{\omega}, \boldsymbol{\omega}')$ is infinite provided that the two particles overlap and vanishes otherwise.

In addition we consider that the system is confined by a planar smooth hard wall, which we take to be perpendicular to the z-direction and to be located at $z = 0$, such that only the halfspace $z > 0$ is accessible to the particles. Hence the interaction between the hard planar wall and a platelet is described by an external potential,

$$V_{\text{ext}}(z, \theta) = \begin{cases} \infty & z < R \sin\theta \\ 0 & \text{otherwise.} \end{cases} \tag{2.1}$$

where θ is the angle between the z-direction (normal to the wall) and the particle orientation $\boldsymbol{\omega}$ (normal to the platelet), which we can choose to be in

the range $0 < \theta < \pi/2$ due to the inflection symmetry of the particles. See Fig. 2.1a for an illustration of the model.

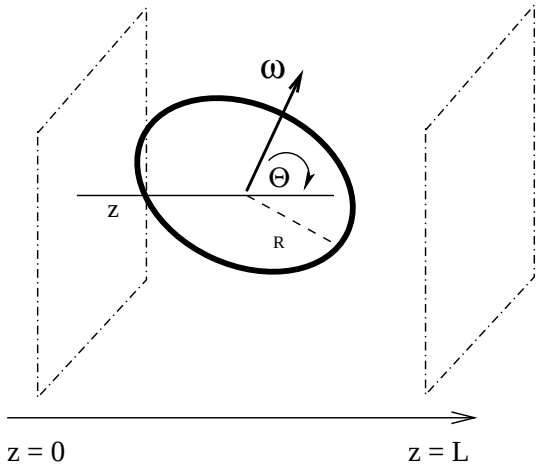

Figure 2.1: Model of hard platelets with radius R and vanishing thickness at a planar hard wall. The angle between the z direction, perpendicular to the wall, and the platelet orientation $\boldsymbol{\omega}$ is denoted by θ. For convenience we also consider a second parallel wall at a distance L.

The one-body density distribution of the platelets is denoted by $\rho(\mathbf{r}, \boldsymbol{\omega})$. As bulk parameters we use the scaled density ρR^3, where R is the radius of a platelet, and the normalisation is chosen such that $\rho = \frac{1}{4\pi} \int d\mathbf{r} d\boldsymbol{\omega}\, \rho(\mathbf{r}, \boldsymbol{\omega})$. As we do not expect biaxiality to occur, we assume invariance with respect to rotations around the z axis, as well as translational invariance in the x and y directions. The remaining relevant angle θ is that between the orientation $\boldsymbol{\omega}$ and the z axis, see Fig. 2.1a. It follows that the (number) density distribution $\rho(\mathbf{r}, \boldsymbol{\omega}) = \rho(z, \theta)$.

In two chapters, we will go beyond this model: in chapter 5 we compare our results for capillary nematization of hard platelets with those for (infinitely thin) hard rods. For this system, the same geometry as above will be assumed. In chapter 6, we will investigate platelets and rods at *finite* thickness, where we restrict ourselves to bulk systems. Relevant quantities are defined in this chapter.

2.2 Density functional theory

In this section, we start with a short overview of (classical) density functional theory (DFT). For more information, we refer the reader to the literature on DFT, see e.g. [39]. A special version of DFT used in this thesis, the fundamental measure theory (FMT), will be discussed in section 2.3.

DFT is a theoretical method which is an ideal tool to investigate inhomogeneous systems. Originally developed by Hohenberg and Kohn [40, 41] to describe quantum mechanical systems, it was later modified by Mermin [42] to allow the application on classical systems. The basic idea is the minimisation of a grand potential functional $\tilde{\Omega}[\rho]$, which depends on the one-particle density ρ. One can show that $\tilde{\Omega}[\rho]$ is a unique functional of the external potential V_{ext} and a function of temperature T, volume V and chemical potential μ.

From $\tilde{\Omega}[\rho]$ follows the equilibrium density profile ρ_{eq} for nonspherical particles via

$$\frac{\delta\tilde{\Omega}[\rho]}{\delta\rho(\mathbf{r},\boldsymbol{\omega})} = 0, \tag{2.2}$$

and hence

$$\tilde{\Omega}[\rho_{eq}] = \Omega, \tag{2.3}$$

where Ω is the equilibrium grand potential.

The grand potential for particles with translational and orientational degrees of freedom, denoted by $\mathbf{r}$ and $\boldsymbol{\omega}$, is given by

$$\tilde{\Omega}([\rho],\mu) = F_{\text{id}}[\rho] + F_{\text{exc}}[\rho] + \int d\mathbf{r} \int \frac{d\boldsymbol{\omega}}{4\pi}\rho(\mathbf{r},\boldsymbol{\omega})\left(V_{\text{ext}}(\mathbf{r},\boldsymbol{\omega}) - \mu\right), \tag{2.4}$$

where $F_{\text{exc}}[\rho]$ is the excess (over ideal gas) contribution to the total (Helmholtz) free energy that arises from inter-particle interactions, $V_{\text{ext}}(\mathbf{r},\boldsymbol{\omega})$ is an external potential, μ is the chemical potential, and the ideal gas (Helmholtz) free energy functional for uniaxial rotators is given by

$$F_{\text{id}}[\rho] = k_B T \int d\mathbf{r} \int \frac{d\boldsymbol{\omega}}{4\pi}\rho(\mathbf{r},\boldsymbol{\omega})\left(\ln(\rho(\mathbf{r},\boldsymbol{\omega})\Lambda^3) - 1\right), \tag{2.5}$$

where k_B is Boltzmann's constant, T is the absolute temperature, and Λ is the (irrelevant) thermal wavelength; the dependence on volume V has been suppressed in the notation. Equation (2.2) can be rewritten, using (2.4), as an Euler-Lagrange equation

$$k_B T \ln(\rho(\mathbf{r},\boldsymbol{\omega})\Lambda^3) - k_B T c_1([\rho],\mathbf{r},\boldsymbol{\omega}) + V_{\text{ext}}(\mathbf{r},\boldsymbol{\omega}) = \mu, \tag{2.6}$$

where $c_1([\rho], \mathbf{r}, \boldsymbol{\omega}) = -(k_B T)^{-1} \delta F_{\text{exc}}[\rho]/\delta\rho(\mathbf{r}, \boldsymbol{\omega})$ is the one-body direct correlation functional.

The problem is that $F_{\text{exc}}[\rho]$ is not known in general and exact results are only available for special cases (e.g. hard rods in one dimension [1]), so that one has to rely on approximations when using DFT.

One systematic way to write down the excess free energy functional $F_{\text{exc}}[\rho]$ is to expand it in a virial series,

$$\begin{aligned} F_{\text{exc}}[\rho] = &- \frac{1}{2} \int d\mathbf{r} \int \frac{d\boldsymbol{\omega}}{4\pi} \int d\mathbf{r}' \int \frac{d\boldsymbol{\omega}'}{4\pi} \rho(\mathbf{r}, \boldsymbol{\omega}) \rho(\mathbf{r}', \boldsymbol{\omega}') f(\mathbf{r} - \mathbf{r}', \boldsymbol{\omega}, \boldsymbol{\omega}') \\ &+ \frac{1}{6} \int d\mathbf{r} \int \frac{d\boldsymbol{\omega}}{4\pi} \int d\mathbf{r}' \int \frac{d\boldsymbol{\omega}'}{4\pi} \int d\mathbf{r}'' \int \frac{d\boldsymbol{\omega}''}{4\pi} \rho(\mathbf{r}, \boldsymbol{\omega}) \rho(\mathbf{r}', \boldsymbol{\omega}') \rho(\mathbf{r}'', \boldsymbol{\omega}'') \\ &\times f(\mathbf{r} - \mathbf{r}', \boldsymbol{\omega}, \boldsymbol{\omega}') f(\mathbf{r} - \mathbf{r}'', \boldsymbol{\omega}, \boldsymbol{\omega}'') f(\mathbf{r}' - \mathbf{r}'', \boldsymbol{\omega}', \boldsymbol{\omega}'') + O(\rho^4) \end{aligned} \tag{2.7}$$

where $f(\mathbf{r}, \boldsymbol{\omega}, \boldsymbol{\omega}') = \exp(-\beta V(\mathbf{r}, \boldsymbol{\omega}, \boldsymbol{\omega}')) - 1$ is the Mayer function that for hard bodies is -1 if the two particles overlap and vanishes otherwise. In practice, one has to resort to approximations and Onsager's theory relies on truncating Eq. (2.7) after second order in density. This is known to be a good approximation for thin rods; we will discuss how it fares for platelets below.

Several approximations for $F_{\text{exc}}[\rho]$ for platelets have been proposed, see e.g. [43]. Ref. [44] gives an FMT for parallel hard cubes; Ref. [45,46] investigate the properties of the Zwanzig model (which uses restricted orientations), and Ref. [47] is devoted to the role of three-body correlations in a system of hard rectangles. The FMT functional for platelets used in this thesis relies on the theory of Ref. [38] for a ternary mixture of hard spheres, needles, and platelets.

2.3 Fundamental Measure Theory

The Fundamental Measure Theory (FMT) was originally derived for additive hard sphere mixtures [48]. An extension to arbitrarily shaped convex bodies was proposed in Refs. [49, 50], which yields the correct second virial coefficients, but gives only an approximation for the Mayer bond(s), and hence the second order contribution in density to the excess free energy. This is insufficient to describe e.g. nematic ordering (see e.g. Ref. [51] for a discussion). The theory of Ref. [38] remedies this deficiency for the case of platelets, and hence possesses the correct contribution of second order in density, and also features a term of third order in density, but no higher order terms. The

absence of higher order terms is intimately connected to the scaled-particle roots of the approach and can in particular be traced back to the vanishing volume of the particles. The third order term is different from the exact third virial contribution, the third order term of Eq. (2.7). It is non-vanishing (and constant) for cases with common triple intersection of the three particles involved. Global prefactors are used to compensate for the "lost cases" [52, 53] in order to yield reasonable values for the third virial coefficients. A detailed discussion is given in Ref. [38].

The excess free energy functional is expressed as an integral over space and (in the case of platelets) twice over director space,

$$\beta F_{\rm exc}[\rho] = \int d\mathbf{r} \int \frac{d\boldsymbol{\omega}}{4\pi} \int \frac{d\boldsymbol{\omega}'}{4\pi} \Phi(\{n_i^\nu\}), \tag{2.8}$$

where the (reduced) free energy density, Φ, is a function of a set of the weighted densities n_i^ν, where ν and i label the type of weighted density (detailed below).

2.3.1 Application to hard platelets

For pure infinitely thin hard platelets the free energy density is given by

$$\Phi(\{n_i^\nu\}) = n_1^{DD}(\boldsymbol{\omega}) n_2^D(\boldsymbol{\omega}) + \frac{1}{24\pi} n_2^D(\boldsymbol{\omega}) n_2^{DDD}(\boldsymbol{\omega}, \boldsymbol{\omega}') n_2^D(\boldsymbol{\omega}'), \tag{2.9}$$

where the first term on the r.h.s. recovers the exact second virial contribution. The weighted densities are related to the bare one-body density, $\rho(\mathbf{r}, \boldsymbol{\omega})$, via

$$n_2^D(\mathbf{r}, \boldsymbol{\omega}) = w_2^D(\mathbf{r}, \boldsymbol{\omega}) * \rho(\mathbf{r}, \boldsymbol{\omega}), \tag{2.10}$$

$$n_1^{DD}(\mathbf{r}, \boldsymbol{\omega}') = \int \frac{d\boldsymbol{\omega}}{4\pi} w_1^{DD}(\mathbf{r}, \boldsymbol{\omega}; \boldsymbol{\omega}') * \rho(\mathbf{r}, \boldsymbol{\omega}), \tag{2.11}$$

$$n_2^{DDD}(\mathbf{r}; \boldsymbol{\omega}; \boldsymbol{\omega}') = \int \frac{d\boldsymbol{\omega}''}{4\pi} w_2^{DDD}(\mathbf{r}, \boldsymbol{\omega}''; \boldsymbol{\omega}; \boldsymbol{\omega}') * \rho(\mathbf{r}, \boldsymbol{\omega}''), \tag{2.12}$$

where $*$ denotes the three-dimensional convolution, and the weight functions are given by

$$w_1^D(\mathbf{r}, \boldsymbol{\omega}) = \delta(R - |\mathbf{r}|)\delta(\mathbf{r} \cdot \boldsymbol{\omega})/8, \tag{2.13}$$

$$w_2^D(\mathbf{r}, \boldsymbol{\omega}) = 2\Theta(R - |\mathbf{r}|)\delta(\mathbf{r} \cdot \boldsymbol{\omega}), \tag{2.14}$$

$$w_1^{DD}(\mathbf{r}, \boldsymbol{\omega}; \boldsymbol{\omega}') = \frac{2}{R} |\boldsymbol{\omega} \cdot (\boldsymbol{\omega}' \times \mathbf{r})| w_1^D(\mathbf{r}, \boldsymbol{\omega}), \tag{2.15}$$

$$w_2^{DDD}(\mathbf{r}, \boldsymbol{\omega}; \boldsymbol{\omega}'; \boldsymbol{\omega}'') = \frac{8}{\pi} |\boldsymbol{\omega} \cdot (\boldsymbol{\omega}' \times \boldsymbol{\omega}'')| w_2^D(\mathbf{r}, \boldsymbol{\omega}), \tag{2.16}$$

where $\Theta(\cdot)$ is the unit step (Heaviside) function and $\delta(\cdot)$ is the Dirac distribution. We have kept the notation of Ref. [38] where the upper index D refers to the species (disks), and its number of appearances indicates the number of particle orientations that appear in the definition of the weight functions, Eqs. (2.13)- (2.16). We will initially restrict ourselves to the case of infinitely thin hard platelets. In chapter 7, we will investigate hard platelets with finite thickness. Then, additional weight functions to those given above will appear.

2.3.2 Application to hard rods

As for platelets, we will firstly restrict ourselves to infinitely thin hard rods, thus $L/D \to \infty$, where L denotes the length L and D the width of the rods. In chapter 6, we will drop this restriction and look at hard rods with finite thickness. Although the Onsager limit has yet been discussed (see the first term of (2.7)), we repeat it here in the FMT formalism to establish a basis for the investigations in chapter 6.

However, the excess free energy in the Onsager limit of hard rods is given by an integral over a free energy density Φ as in the case of platelets,

$$\beta F_{\text{exc}}[\rho] = \int d\mathbf{r} \int \frac{d\boldsymbol{\omega}}{4\pi} \Phi(\{n_i^\nu\}). \tag{2.17}$$

Note that we integrate here only once over director space (in contrast to Eq. (2.8) for platelets, where three particle correlations were involved). The reason is that for rods the Onsager limit is sufficient to describe the IN transition. The free energy density Φ reads as

$$\Phi = n_1 n_2^{NN} \tag{2.18}$$

with the weighted densities n_1 and n_2^{NN},

$$n_1^N(\mathbf{r}, \boldsymbol{\omega}) = w_1^N(\mathbf{r}, \boldsymbol{\omega}) * \rho(\mathbf{r}, \boldsymbol{\omega}), \tag{2.19}$$

$$n_2^{NN}(\mathbf{r}, \boldsymbol{\omega}') = \int \frac{d\boldsymbol{\omega}}{4\pi} w_2^{NN}(\mathbf{r}, \boldsymbol{\omega}, \boldsymbol{\omega}') * \rho(\mathbf{r}, \boldsymbol{\omega}), \tag{2.20}$$

where $*$ again denotes the three-dimensional convolution, and the weight

functions are given by

$$w_2^{NN}(\mathbf{r},\boldsymbol{\omega},\boldsymbol{\omega'}) = 4D\sqrt{1-(\boldsymbol{\omega}\boldsymbol{\omega'})^2}\int_{-L/2}^{L/2} dl\delta(\vec{r}+l\boldsymbol{\omega}), \tag{2.21}$$

$$w_1^{N}(\mathbf{r},\boldsymbol{\omega}) = \frac{1}{4}\int_{-L/2}^{L/2} dl\delta(\vec{r}+l\vec{\Omega}). \tag{2.22}$$

$$\tag{2.23}$$

The upper index N again refers to the species under consideration (here denoted as needles) to be consistent with Ref. [54] and [38].

2.4 Numerical procedure

To obtain the weight functions and hence the weighted densities in planar geometry for platelets, we integrate over the in-plane coordinates x, y in Eqs. (2.10)-(2.12), assuming azimuthal symmetry such that the density distribution only depends on z and θ, see Sec. VII of Ref. [38] for explicit results. Our numerical implementation of Eq. (2.6) uses free minimisation, i.e. no *a priori* form of $\rho(z,\theta)$ is assumed. For practical reasons, we add a second hard wall, such that the walls are located at $z = 0$ and $z = L$, with typically $L/R = 51$, which is large enough to prevent significant capillary effects and on the other hand keeps the numerical effort reasonable. An equidistant grid in the z direction with 20 grid points per particle radius R is used. The angle θ is discredited on a non-equidistant grid with 20 grid points in the interval $[0;\pi/2]$. This adds up to a total of $\approx 2\cdot 10^4$ grid points. The numerical minimisation is performed using molecular dynamics-type simulated annealing [55–57]. Our convergence criterion relies on the norm ϵ defined as the maximum of the standard euclidean vector norm for the difference of the numerical "vector" $\rho(z,\theta = \text{const})$ between two minimisation steps, and we take $\epsilon < 10^{-6}$ as the threshold. For low values of the scaled chemical potential μ^*, and hence far away from the coexistence region, $\sim 10^2$ steps were sufficient to obtain convergence. At higher values of μ^*, close to its value at IN coexistence, up to $\sim 10^5$ steps were necessary to obtain convergence.

We next define some order quantities widely used when investigating inhomogeneous systems. The first one is the orientation-averaged density profile, which measures the density of platelet midpoints at position z, and is

obtained from the full density profile as

$$\rho(z) = \int_0^{\pi/2} d\theta \sin(\theta)\rho(z,\theta). \tag{2.24}$$

To assess the degree of local nematic order we use the nematic order parameter profile, defined as

$$S(z) = [\rho(z)]^{-1} \int_0^{\pi/2} d\theta \sin(\theta)\rho(z,\theta)P_2(\cos\theta), \tag{2.25}$$

where $P_2(x) = (3x^2 - 1)/2$ is the second order Legendre polynomial. The normalisation is such that $S = 0$ indicates isotropic states, while $S = 1$ indicates parallel alignment of particles i.e. the nematic state.

Chapter 3

Platelets in bulk and at a single hard wall

In this chapter we investigate the behaviour of hard platelets in bulk, where we calculate the IN transition and the equation of state, and at a single hard wall. In the later case, we are interested in the question whether the nematic phase of the platelets wets the hard wall or not. We compare our results obtained by FMT with that from Monte Carlo (MC) computer simulations, which were performed by M. Dijkstra from Utrecht University and with theoretical calculations for the Onsager limit, which were done by R. van Roij, also from Utrecht University. A short account of this work has been published as part of Ref. [58].

3.1 Bulk properties of hard platelets

For the bulk IN transition we obtain from FMT the value of the chemical potential at coexistence, density of the isotropic and the nematic phase, and order parameter in the isotropic and the nematic phase, as $\mu^*_{\rm coex} = 5.004$, $\rho_I R^3 = 0.419$, $\rho_N R^3 = 0.469$, $S_N = 0.531$, $S_I = 0.045$, respectively. These values differ slightly from those of the bulk treatment reported in [38], where no z-dependence was resolved and hence higher angular resolution with 100 grid points could be used, resulting in [38] $\rho_I R^3 = 0.418$, $\rho_N R^3 = 0.460$, $S_N = 0.492$, $S_I = 0$. Both data sets are in good agreement with the simulation results [7], which are $\rho_I R^3 = 0.460$, $\rho_N R^3 = 0.498$ and $S_N = 0.45 - 0.55$. Second order virial theory gives $\rho_I R^3 = 0.667$, $\rho_N R^3 = 0.849$ and $S_N = 0.78$, hence it correctly predicts a first order transition, but overestimates both the density jump and the order parameter at coexistence. Fig. 3.1a shows the

order parameter as a function of the density to illustrate these results. In Fig. 3.1b we plot the equation of state, i.e. the pressure P as a function of the scaled bulk density ρR^3. For comparison, we plot the equation of state obtained from isobaric MC simulations using very long runs of up to 10^6 cycles for a system of 500 particles. Fig. 3.1b shows that these simulation results are consistent with simulation results from earlier studies [6,59,60] and are very well reproduced by the FMT approach. Onsager theory again gives only qualitatively accurate results. In the isotropic phase, it underestimates the pressure, while in the nematic phase it overestimates the pressure, which is due to the too large coexistence densities leading to too large a density in the coexisting nematic phase. Note also that the slope $dP/d\rho$ as predicted by the Onsager functional is smaller than that of the FMT functional in the nematic phase.

3.2 Free isotropic-nematic interface

At bulk IN coexistence a planar interface that separates the isotropic and nematic phases will be stable. The behaviour of such an inhomogeneous systems is conveniently analysed using the orientation averaged density profile $\rho(z)$ as defined in (2.24) and the nematic order parameter profile, defined in (2.25).

We first investigate properties of the free IN interface as obtained from FMT. Fig. 3.2a shows the density profile across the interface for perpendicular alignment of the nematic director with the surface, i.e. such that the platelets tend to lie flat against the free IN interface. The preference for homeotropic anchoring was consistently found by experimental investigations [58] and for the Zwanzig model [37]. The interface is smooth and crosses over monotonically between the densities of the coexisting phases, without any signs of oscillations. We have analysed the asymptotic decay of the density profile into either bulk phase in detail. We expect that for $z \to -\infty$, i.e. on the nematic side of the interface $|\rho(z) - \rho_N| \propto \exp(-|z/\xi_N^\rho|)$, while for $z \to \infty$, i.e. on the isotropic side $|\rho(z) - \rho_I| \propto \exp(-|z/\xi_I^\rho|)$, where ξ_I^ρ and ξ_N^ρ are the correlation lengths in the coexisting I and N phases, respectively, and the upper index is a reminder of their relationship to $\rho(z)$. We hence plot in the insets of Fig. 3.2a $\ln|\rho(z) - \rho_I|$ on the isotropic side and $\ln|\rho(z) - \rho_N|$ on the nematic side of the interface as a function of z. The observed linear dependence confirms the expectation, and from the slopes we obtain $\xi_I^\rho/R = 1.32$ and $\xi_N^\rho/R = 1.35$. Results for $\rho(z)$ for Onsager theory (provided by R. van Roij, Utrecht university) are shown in Fig. 3.2b and

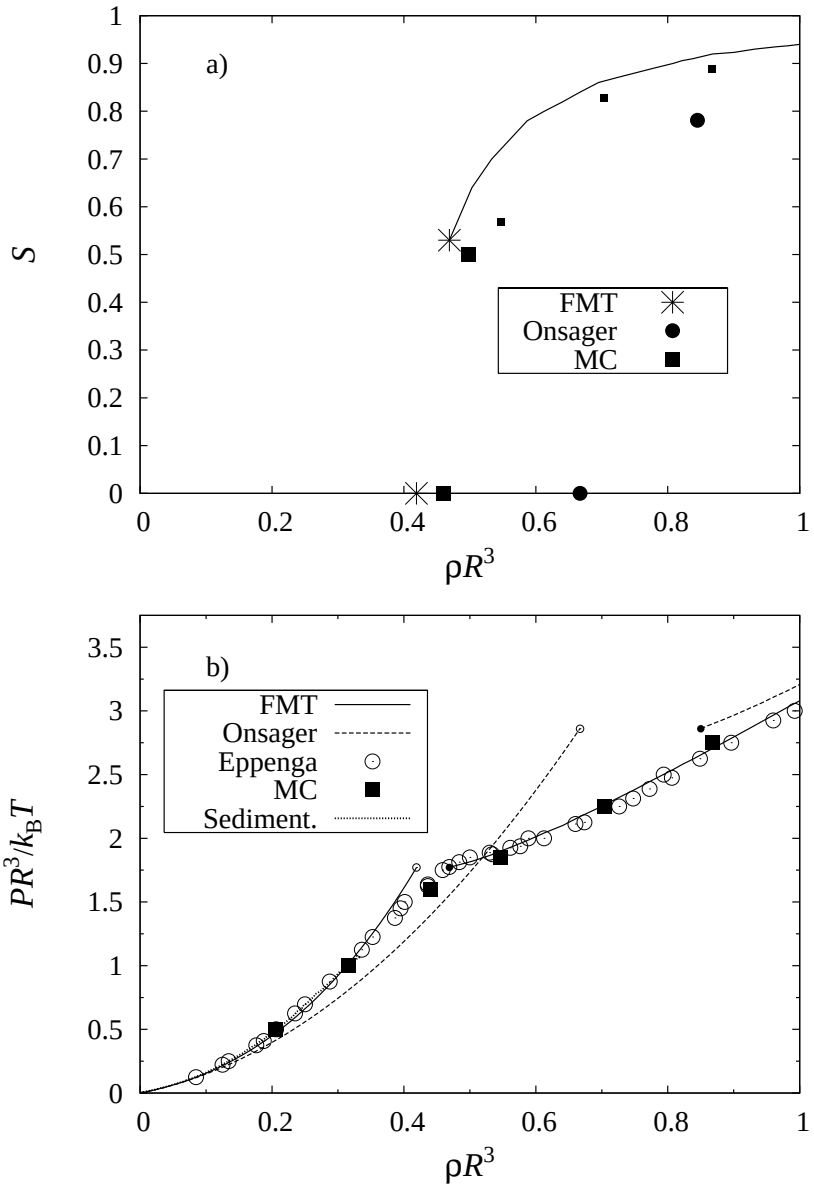

Figure 3.1: a) Nematic order parameter S and bulk density ρR^3 at coexistence as obtained from FMT (big stars), MC simulations (big squares) and Onsager theory (closed circles). Also shown is S as a function of ρR^3 in the nematic phase from FMT (full line) and MC simulation (small squares, to distinguish from the big squares indicating the IN transition). b) Scaled pressure PR^3/k_BT as a function of the bulk density ρR^3 as obtained from FMT (full line), MC simulations (black squares) and Onsager theory (dashed line). Also shown are the MC simulation results of Ref. [6] (open circles) and those obtained from sedimentation profiles, see Ref. [60] (dotted line). The small open and closed circles indicate the theoretical results for the isotropic and nematic coexisting phases, respectively.

will be discussed below. Fig. 3.2c shows the corresponding order parameter profile as obtained from FMT. Again we have analysed the asymptotic decay of the profile and find that the order parameter decays for $z \to -\infty$ as $|S(z) - S_N| \propto \exp(-|z/\xi_N^S|)$, where $\xi_N^S/R = 1.33$, and for $z \to \infty$ as $|S(z) - S_I| \propto \exp(-|z/\xi_I^S|)$ where $\xi_I^S = 1.28$, see the inset of Fig. 3.2b. We expect that $\xi_I^\rho = \xi_I^S$ and $\xi_N^\rho = \xi_N^S$, and indeed find this to good accuracy to be fulfilled, which demonstrates the internal consistency of our calculations. The fact that $\rho(z)$ and $S(z)$ decay monotonically on either side of the interface is in contrast to what is found in Onsager theory, where indeed weak oscillations are apparent on the *isotropic* side of the interface. We will discuss the relationship of the asymptotic decay at the free IN interface with that at a wall in more detail in Sec. 3.3.

Results from Onsager theory are plotted in Figs. 3.2b (density $\rho(z)$) and d (order parameter $S(z)$). In contrast to the latter, we find weak oscillations at the isotropic side of the free IN-interface in the density and order-parameter profiles. These oscillations are clearly visible in the insets on the nematic side of Fig. 3.2 b and d, where we plot $\rho(z)$ and $S(z)$ on a logarithmic scale. For more details see the discussion below in Sec. 3.3.

To illustrate the properties of the free IN interface further, we plot in Fig. 3.3 $\rho(z, \theta = \text{const})$ as a function of z/R for seven different values of θ. We find that for $\theta \to \pi/2$ the density in the nematic phase is lower than in the isotropic phase, which is due to the ordering in the nematic phase around the nematic director at $\theta = 0$; this causes lower densities around $\theta = \pi/2$. Furthermore, the inset of Fig. 3.3 shows $\rho(z = \text{const}, \theta)$ as a function of θ for three different values of z/R, where $z/R = -10$ is on the nematic side, $z/R = 10$ is on the isotropic side of the interface, and $z = 0$ is at the Gibbs dividing surface. The cross-over from a nematic to an isotropic orientation distribution is clearly visible.

We explore in the following the repercussions of the interfacial properties of the free IN interface on the adsorption behaviour of platelets at a hard wall.

3.3 Behaviour of platelets at a hard wall

The hard wall constitutes a basic yet realistic model for a substrate, e.g. a container wall, that a colloidal dispersion is exposed to. Although only constituting a hard core constraint (see Eq. (2.1) for the precise definition of the external potential), the hard wall induces coupling of orientation and translation degrees of freedom, i.e. the restriction in available orientations de-

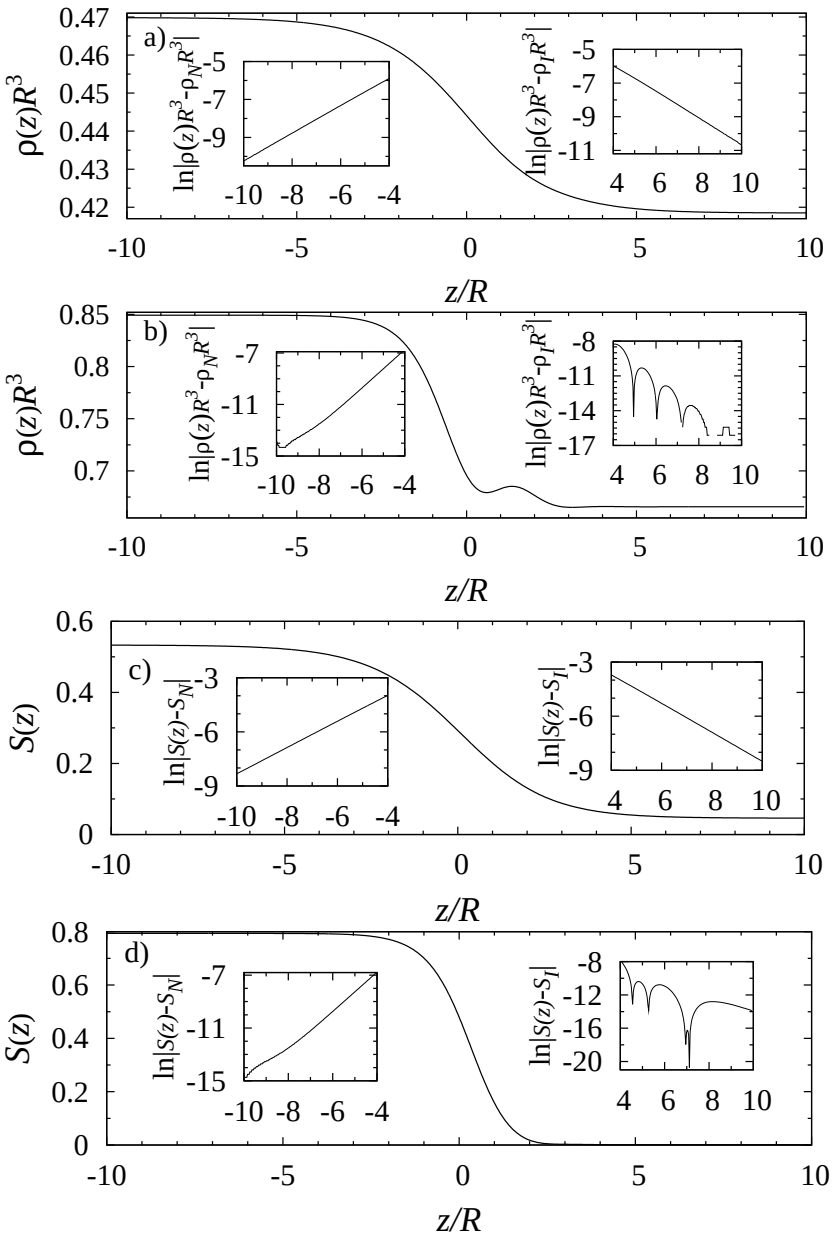

Figure 3.2: a) Density profile $\rho(z)R^3$ across the free IN interface as obtained from FMT. The insets show $\ln|(\rho(z)R^3) - \rho_{I,N}R^3|$. b) Density profile $\rho(z)R^3$ across the free IN interface as obtained from Onsager theory. The insets show $\ln|(\rho(z)R^3) - \rho_{I,N}R^3|$. c) Order parameter profile $S(z)$ across the free IN interface from FMT. The insets show $\ln|(S(z)) - S_{I,N}|$. d) Order parameter profile $S(z)$ across the free IN interface from Onsager theory. The insets show $\ln|(S(z)) - S_{I,N}|$.

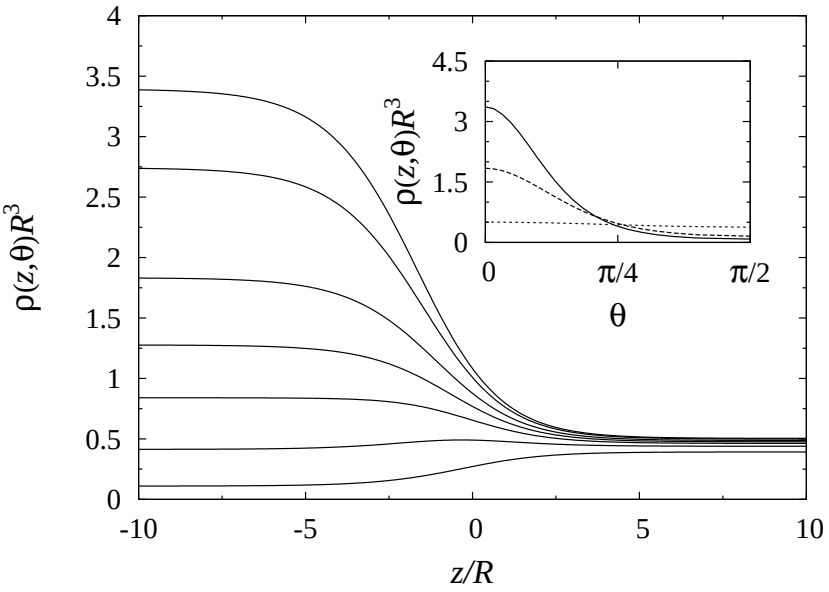

Figure 3.3: Variation of $R^3\rho(z,\theta)|_{\theta=\text{const}}$ across the free IN interface for seven different values of $\theta \in [0, \pi/2]$, namely $\theta = 0, 0.2, 0.36, 0.47, 0.58, 0.78, 1.57$ (from top to bottom). The inset shows $R^3\rho(z,\theta)|_{z=\text{const}}$ for $z = -10, 0, 10$ (from top to bottom, relating to the left side of the inset).

pends on the distance of the particle to the wall. Fig. 3.4a shows orientation-averaged density profiles, $\rho(z)R^3$ as defined in Eq. (2.24), obtained from FMT for a range of chemical potentials approaching bulk IN coexistence. For low values of μ^*, and correspondingly low values of the bulk density, ρR^3, a pronounced "correlation hole" is apparent near the wall [35]. This originates from the reduction in available configurations due to overlap of the platelet with the wall. At $z = R$ there is a sharp cusp, followed by weak oscillations for larger distances z. Quite unexpectedly but consistent with the monotonic decay at the free IN interface these oscillations disappear upon increasing μ^*. A further shoulder appears very close to the wall, $z \sim 0.5R$, which develops into an independent peak that grows in size and becomes eventually larger than the cusp at $z = R$. A pronounced wetting film grows upon approaching bulk IN coexistence. The film decays from a plateau with a value that is very similar to the density of the coexisting nematic phase smoothly to the value of the isotropic bulk. To demonstrate the similarity between the wetting film at the hard wall and the free IN interface, we superimpose the density profile of the free IN interface in Fig. 3.4a. We show results from Onsager theory in Fig. 3.4b, where we have plotted density profiles for different bulk densities $\rho(z)R^3$. The profiles for small bulk densities are very similar to those obtained from FMT. With increasing density, a nematic wetting layer develops. While the behaviour close to the wall agrees with that found in FMT, we find the wetting films are more pronounced compared to FMT and MC simulations. This is consistent with the larger density jump at the IN-transition.

In order to test the theoretical results M. Dijkstra has carried out NVT MC simulations using very large system sizes of up to $N = 7 \cdot 10^4$ hard platelets confined between two planar hard walls. As the interfacial tension between the isotropic and nematic phase is very low, we needed large (lateral) wall areas in order to stabilise the nematic film against thermal fluctuations. Moreover large wall separations were needed to prevent capillary nematization. The density profiles resulting from the MC simulations are shown in Fig. 3.4c. Note that the bulk values of the density profiles are different from those considered in the DFT calculations. The density profiles from MC simulations confirm the existence of a correlation hole close to the wall and the cusp at $z = R$ for low densities. With increasing density, this peak vanishes and is replaced by a peak at $z \sim 0.5R$, in agreement with FMT results. The growing wetting film is somewhat more diffuse than that found by FMT. We attribute this to the presence of additional (capillary wave) fluctuations in the simulations that are not captured in either DFT. We investigate the asymptotic decay of correlations in more detail below.

In Fig. 3.5a we show the order parameter profiles at the hard wall from FMT for the same statepoints as considered in Fig. 3.4a. Upon approaching the wall $S(z \to 0)$ approaches unity, as a platelet with small separation from the wall must be well aligned with the wall to avoid overlap. For low bulk densities there is a minimum of $S(z)$ near $z \sim 2R$. Strikingly, upon increasing the chemical potential a growing zone of nematic order is found. This confirms that indeed the film of high density possesses nematic order. Fig. 3.5b shows order parameter profiles at the hard wall as obtained from Onsager theory for the same bulk densities as considered in Fig. 3.4b. Again results from FMT and Onsager are very similar for small densities. A strong pronounced nematic wetting layer is found for bulk densities close to IN coexistence. Corresponding results from MC simulations are shown in Fig. 3.5c. Although the MC data contain some statistical noise and the minimum in $S(z)$ is not found in the simulations, the overall agreement to the FMT results is striking.

Fig. 3.6 shows the asymptotic behaviour of $\rho(z)$ for large distances from the wall for three different (bulk) densities as obtained from FMT (a), Onsager (b) and MC simulations (c). To scrutinise the behaviour we plot $\ln|\rho(z)R^3 - \rho R^3|$, which allows to observe oscillations with small amplitude more easily than a linear plot does. Note that at zeros of $|\rho(z)R^3 - \rho R^3|$ its logarithm is $-\infty$. For numerical reasons, the curves in Fig. 3.6 display only a finite negative minimum value; these (relatively) deep local minima correspond to the zeros of $\rho(z)$. While the first minimum is due to the initial increase of the density from the wall, the subsequent minima stem from oscillations of the density profile $\rho(z)$ that extend into the bulk. Hence the monotonic decay of the upper profiles in Fig. 3.6a indicates that the oscillations disappear upon increasing density. This finding is supported by the MC simulations, although in Fig. 3.6c for $z/R > 3.5$ the statistical errors are considerable. In contrast to this scenario, Onsager theory predicts oscillations over the full range of densities in the isotropic phase, as can be seen in Fig. 3.6b. The oscillations move away from the wall with increasing density, but do not disappear. In Fig. 3.7a and b we show the results for the order parameter $S(z)$ obtained from FMT (corresponding to Fig. 3.6a) and Onsager theory (corresponding to Fig. 3.6b), respectively. Again, we find disappearance of oscillations for higher densities from FMT, while Onsager theory shows oscillations over the full range of densities.

The nature of the wetting scenario can be analysed in more detail by

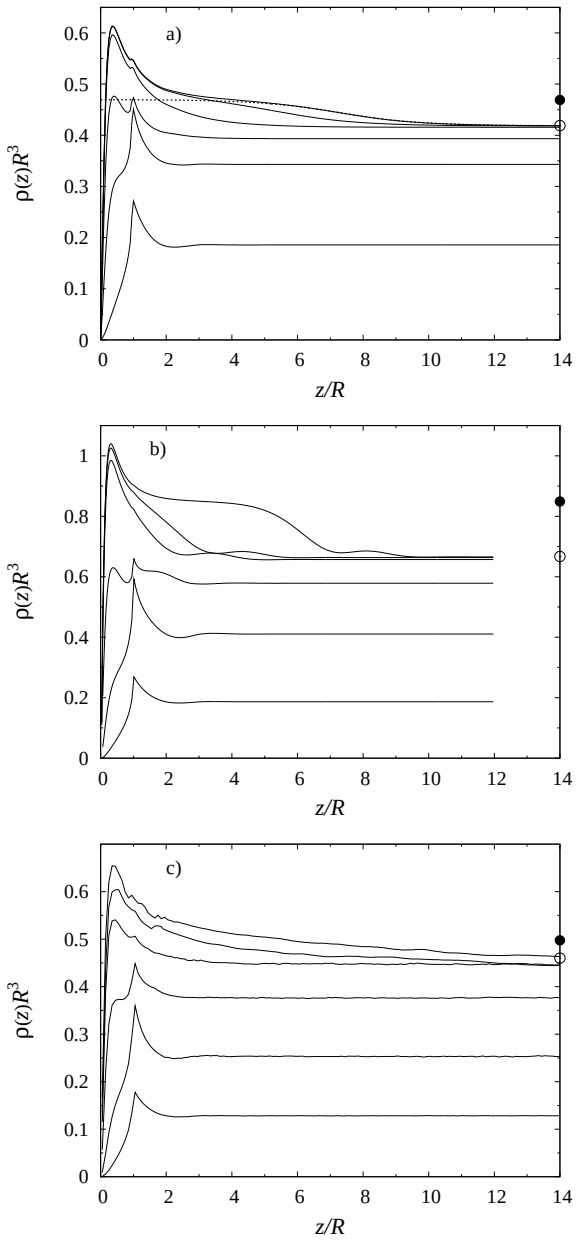

Figure 3.4: a) Density profiles from FMT as a function of the distance from the wall, $\rho(z)R^3$, for values of the scaled (bulk) density $\rho R^3 = 0.186, 0.343, 0.393, 0.416, 0.4182, 0.4184$ (from bottom to top). The dotted line is the profile across the free IN interface. Bulk isotropic and nematic coexistence densities are indicated by the open and closed circles. b) Density profiles from Onsager theory as a function of the distance from the wall, $\rho(z)R^3$, for values of the scaled (bulk) density $\rho R^3 = 0.187, 0.411, 0.579, 0.657, 0.663, 0.665$ (from bottom to top). Bulk isotropic and nematic coexistence densities are indicated by the open and closed circles. c) Density profiles as a function of the distance from the wall, $\rho(z)R^3$, from MC simulations, for bulk densities $\rho R^3 = 0.125, 0.25, 0.38, 0.45, 0.46, 0.475$ (from bottom to top). Bulk isotropic and nematic coexistence densities are indicated by the open and closed circles.

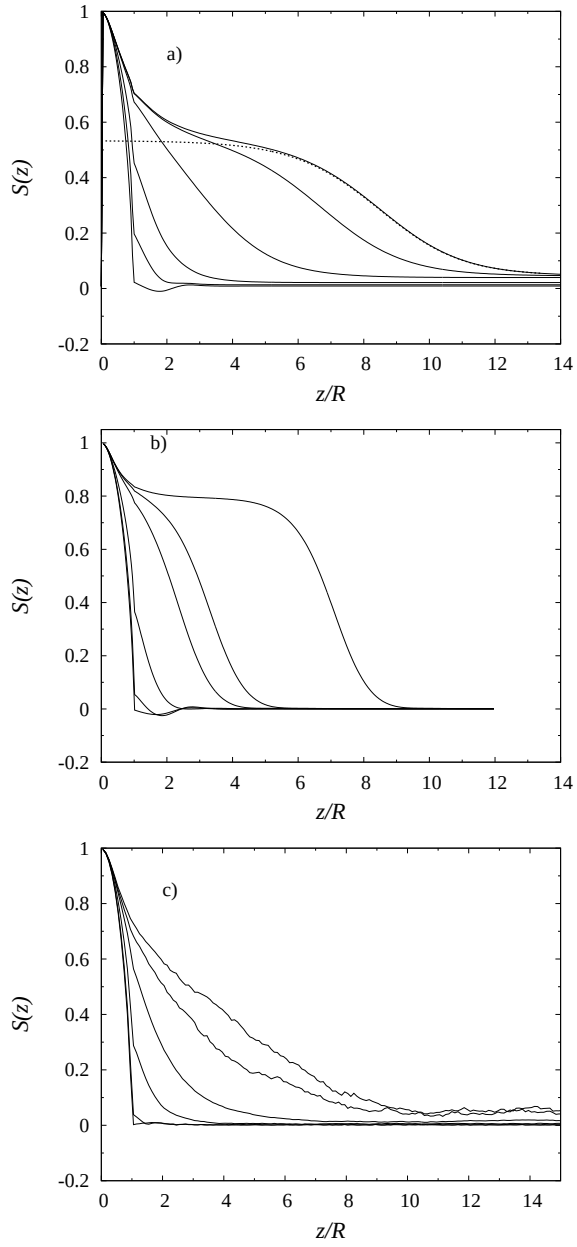

Figure 3.5: a) Nematic order parameter profile from FMT, $S(z)$, as a function of the distance from the hard wall for the same values of ρR^3 as in Fig. 3.4a. The dotted line shows $S(z)$ across the free IN interface. b) Order parameter profiles from Onsager theory, as a function of the distance from the wall. Plotted are results for the same bulk densities as in Fig. 3.4b. c) Nematic order parameter profile, $S(z)$, from MC simulations as a function of the distance from the hard wall, for the same values of ρR^3 as in Fig. 3.4c.

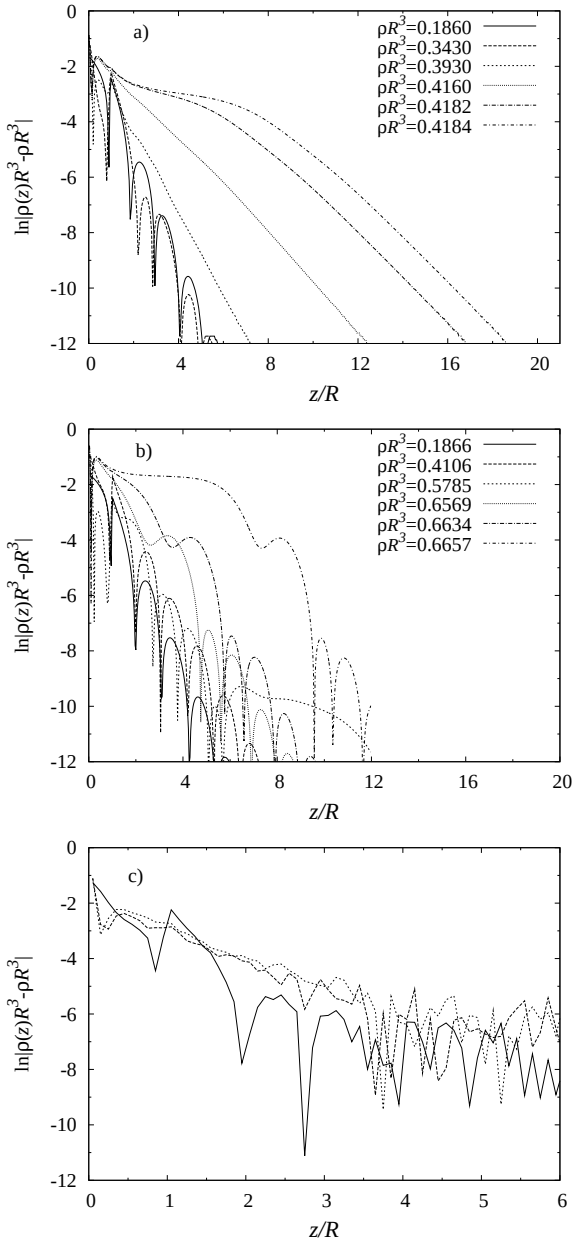

Figure 3.6: a) Variation of $\ln|\rho(z)R^3 - \rho R^3|$ with z/R for the same values of (bulk) density as in Fig. 3.4a, as obtained from FMT. b) Same as a), but from Onsager theory for the (bulk) densities of Fig. 3.4b. c) Same as a) and b), but as obtained from MC simulations for $\rho R^3 = 0.306, 0.444, 0.459$ (from bottom to top).

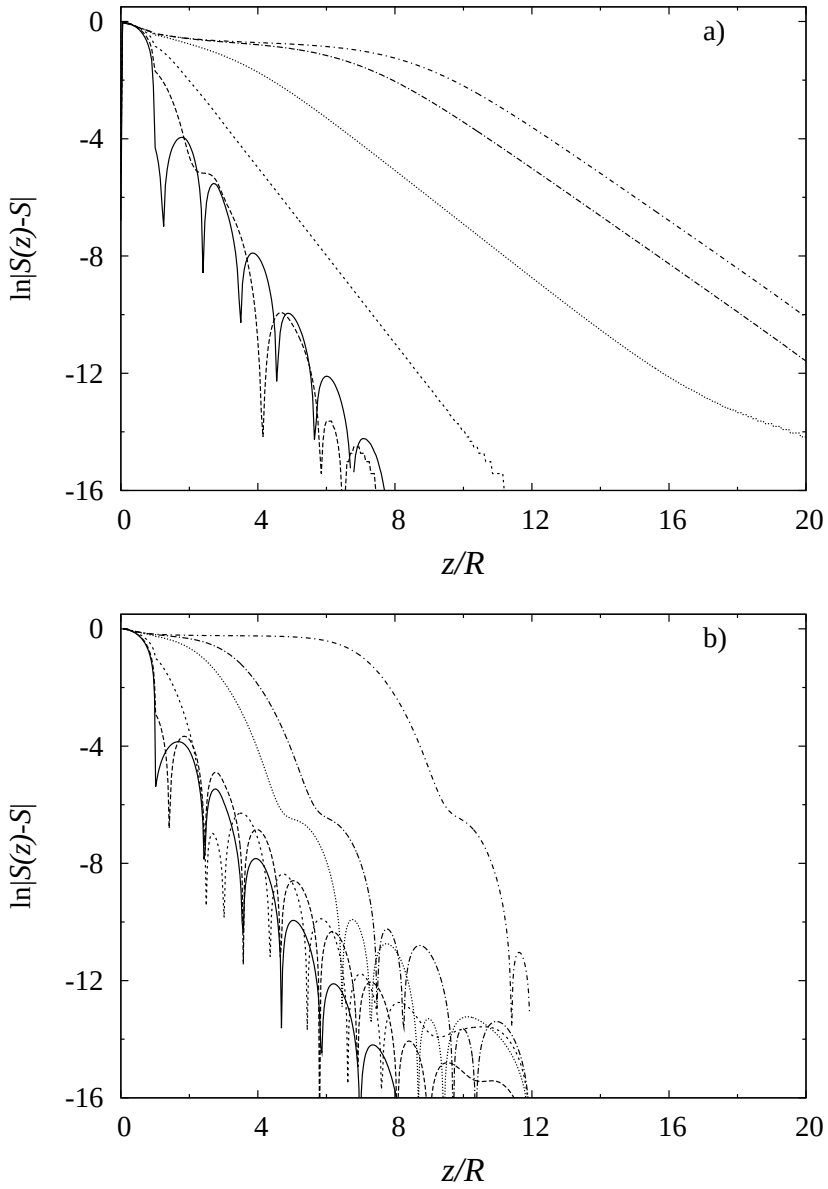

Figure 3.7: a) Variation of $\ln|S(z) - S|$ with z/R from FMT for the same values of ρR^3 as in Fig. 3.6a. b) Variation of $\ln|S(z) - S|$ with z/R from Onsager theory for the same values of ρR^3 as in Fig. 3.6b.

considering the adsorption, either obtained from $\rho(z)$ or from $S(z)$, via

$$\Gamma_\rho = \int_0^\infty dz[\rho(z) - \rho(\infty)], \qquad \Gamma_S = \int_0^\infty dz[S(z) - S(\infty)]. \tag{3.1}$$

In Fig. 3.8a we have plotted Γ_ρ as obtained from FMT as a function of the scaled density ρR^3 in the isotropic and nematic phases. The adsorption is negative for low densities and has a minimum at $\rho R^3 \approx 0.2$. For $\rho R^3 > 0.3$ we find positive values of Γ_ρ, and eventually a sharp increase as ρ approaches its value in the coexistent isotropic phase. This hints of complete wetting of the wall by the nematic phase. In the nematic phase, the adsorption decreases monotonically as a function of ρR^3. This can be explained with increasing nematic ordering in the bulk and hence a loss of structure close to the wall. The film thickness is defined via $d_\rho = \Gamma_\rho/(\rho_N R^3 - \rho_I R^3)$ or $d_S = \Gamma_S/(S_N - S_I)$. The inset of Fig. 3.8a shows d_ρ and d_S as a function of $-\ln(\Delta\mu^*/\mu^*_{\rm coex})$, with $\Delta\mu^* = -(\mu^* - \mu^*_{\rm coex})$. From the fact that we find a linear depence we conclude that the nematic phase wets the wall completely, i.e. that the film thickness diverges as bulk coexistence is approached as

$$d_\rho = \xi^\rho_N \ln(\Delta\mu^*/\mu^*_{\rm coex}) + \text{const}, \qquad d_S = \xi^S_N \ln(\Delta\mu^*/\mu^*_{\rm coex}) + \text{const}, \tag{3.2}$$

which is indeed appropriate for complete wetting in the present case of short-ranged interparticle forces. We find $\xi^\rho_N/R = 1.32$ and $\xi^S_N/R = 1.22$. While the agreement with the data from the decay of the free IN-interface for ξ_ρ is very good, the above given value for ξ_S is slightly smaller than that from the free IN-interface. This can be explained with the larger numerical sensitivity of the order parameter S.

In addition, we consider Young's equation for the contact angle ϑ at which the free IN interface hits the wall,

$$\cos\vartheta = \frac{\gamma_{WI} - \gamma_{WN}}{\gamma_{IN}}, \tag{3.3}$$

where γ_{WN}, γ_{WI} and γ_{IN} are the interfacial tensions between the wall and the nematic phase, between the wall and the isotropic phase, and between the isotropic and the nematic phase respectively. Result for the tensions are obtained from the general definition of the interfacial tension γ of a planar interface,

$$\gamma = (\Omega_{\rm inh} + pV)/A \tag{3.4}$$

where $\Omega_{\rm inh}$ is the grand potential of the inhomogeneous system with the interface, p is the bulk pressure, V is the system volume and A is the lateral

system area (perpendicular to the z-axis). Within DFT $\Omega_{\rm inh}$ is obtained from inserting the equilibrium result for $\rho(z,\theta)$ into Eq. (2.4), i.e. $\Omega_{\rm inh} = \tilde{\Omega}[\rho(z,\theta)]$. Within FMT we find $\gamma_{WN}R^2/k_BT = 0.3327$, and $\gamma_{WI}R^2/k_BT = 0.3391$, and $\gamma_{IN}R^2/k_BT = 0.006656$ (see Sec. 3.2) from Eq. (3.4), which yields $\cos\vartheta \approx 0.96$. Because γ_{IN} is obtained from two numerical similar quantities via (3.4), the resulting value has a relatively large numerical uncertainty. Keeping this in mind when using γ_{IN} in (3.3), the result $\cos\vartheta \approx 0.96$ is consistent with $\vartheta = 0$.

In the simulations thermodynamic integration is used to determine the free energy difference of a bulk system and a system with a wall. The hard wall is approximated by a finite barrier, such that a zero barrier height corresponds to a bulk system and an infinite barrier height to a system with a hard wall [61,62]. This yields the wall tensions γ_{WI} and γ_{WN} and one obtains γ_{IN} via (3.3) assuming $\vartheta = 0$, i.e. the occurrence of complete wetting. The results are $\gamma_{IN}R^2/k_BT = 0.015$ from MC simulations and $\gamma_{IN}R^2/k_BT = 0.051$ from Onsager theory.

In Fig. 3.8b we have plotted the wall interfacial tension $\gamma R^2/k_BT$ as a function of the density far away from the wall $\rho = \rho(\infty)$. At low densities, $\rho R^3 \lesssim 0.3$, we find very good agreement between results from either DFT and the simulations, as well as with the tension obtained from SPT [2], given by

$$\gamma/k_BT = \pi\rho R/4 + \pi\rho^2 R^4/2. \tag{3.5}$$

This SPT result fails, however, to reproduce the maximum of γ below bulk coexistence. There is very good agreement between the location of this maximum ($\rho R^3 \simeq 0.4$) in FMT and MC, whereas Onsager theory locates it far off at $\rho R^3 \simeq 0.6$. The non-monotonic behaviour is accompanied by the growth of the nematic wetting layer, which leads to a reduction of the interfacial tension. In the nematic phase γ decreases as a function of ρR^3, which we can trace back to the increasing nematic order in bulk. The decay predicted by FMT is stronger than that found in the simulations. Although the Onsager functional overestimates the behaviour in the coexistence region significantly, it gives qualitatively similar behaviour.

3.4 Conclusions

In conclusion we have used FMT density functional theory to investigate the free IN interface and the wetting behaviour of hard platelets at a hard wall and compared our results with those obtained from MC simulations and Onsager theory. In our bulk calculations, we find that FMT describes

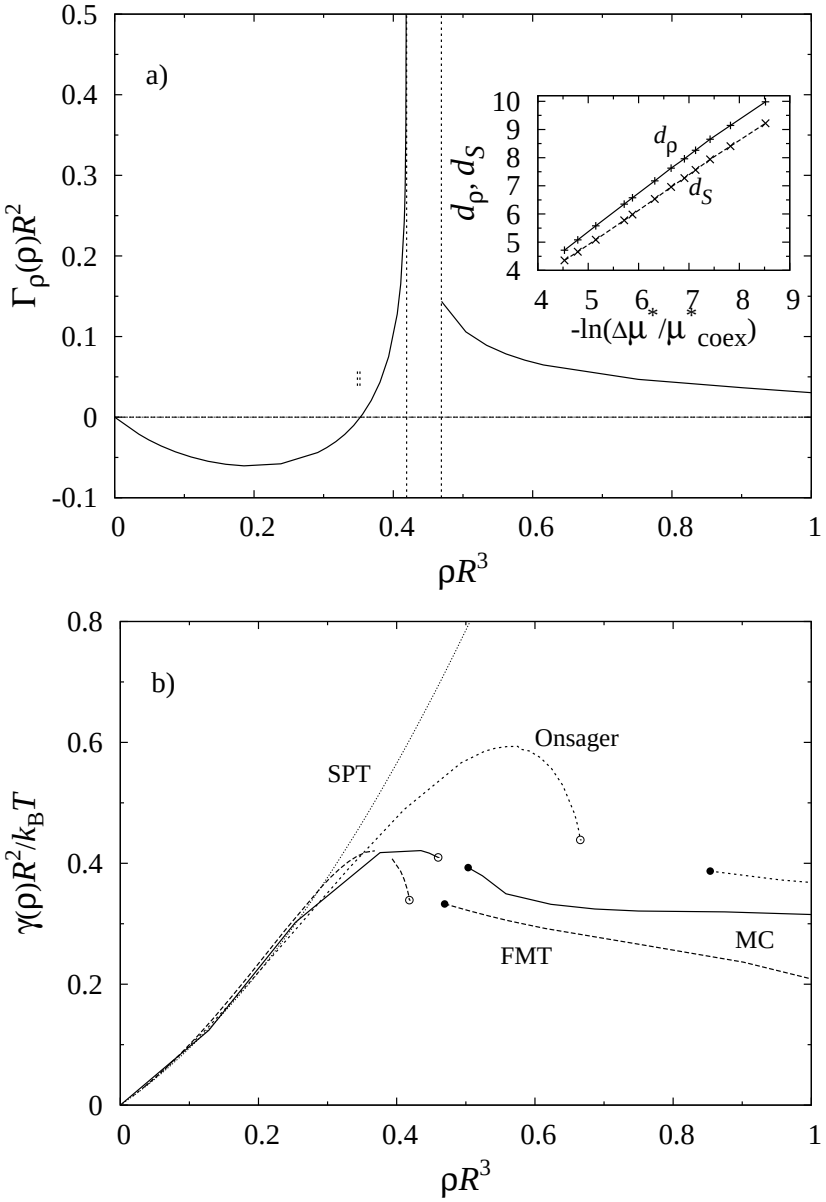

Figure 3.8: a) Adsorption $\Gamma_\rho R^2$ as a function of the density ρR^3, as obtained from FMT. The vertical lines indicate the isotropic and nematic coexistence density. The divergence of Γ_ρ is a signature of complete wetting of the wall. The inset shows FMT results for the thickness d_ρ (upper line) and d_S (lower line) of the nematic wetting film, as defined in the main text, as a function of $-\ln(\Delta\mu^*/\mu_{\rm coex})$. b) Interface tension γ at a hard wall as a function of the scaled bulk density ρR^3, as obtained from FMT (long dashed line), Onsager theory (short dashed line), scaled particle theory (dotted line) and MC simulations (full line). The open and filled circles represent the values at bulk isotropic and nematic coexistence statepoints, respectively, as obtained from FMT, simulations and Onsager theory.

quantities that characterise the IN transition, like the coexistence densities and order parameter at coexistence, very well. The values for the density jump and the order parameter at coexistence are in good agreement with the simulation data. The equation of state in both the isotropic and in the nematic phase agree nicely as obtained from MC simulations and the FMT.

Furthermore, we have investigated the free IN interface in detail. With FMT, we find monotonic decay on either side of the interface. This finding is supported by the simulations, where no oscillations at the hard wall are found for higher densities. Because the asymptotic decay of the hard wall profiles close to the coexistence region is equivalent to that of the free IN interface, this confirms our FMT findings.

Both FMT and simulations predict complete wetting of the hard wall by the nematic phase upon approaching bulk IN coexistence from the isotropic side. For FMT, we have confirmed the complete wetting scenario by analysing the divergence of the adsorption due to the formation of the nematic wetting film and by using Young's equation, which gives $\cos\vartheta = 1$ within the numerical accuracy. Quite surprisingly, FMT and simulations predict disappearing of oscillations of the density profile for higher (bulk) densities.

Comparing the structure of the density profiles obtained from FMT with those from MC simulations, we find extensive similarities. The most eye-catching difference is the decay of the profiles to the bulk value which is somewhat more diffuse in the simulations. We attribute this to the influence of capillary fluctuations on the wetting film, which are not accounted for in the FMT [63, 64]. Finally, we investigated the wall-isotropic interfacial tension with different approaches. The FMT predictions are in close agreement with the simulation data.

Onsager theory gives a qualitatively correct picture. It predicts the IN transition correctly as a first order transition and gives the correct shape of the curves describing the equation of state. Quantitatively, it overestimates the density jump and the order parameter of the IN transition. The pressure in the isotropic phase is underestimated, while the predictions for the nematic phase are too large due to the overestimation of the density jump. This also holds for the interfacial tension. Onsager theory overestimates the value of the wall interfacial tension, but the qualitative behaviour is similar. In the wetting scenario, it gives complete wetting of the wall as also predicted by FMT and simulations. Contrary to the latter, it predicts oscillations for the hard wall profiles over the full range of (isotropic) densities as well as for the isotropic side of the free IN interface.

Possible future investigations are capillary effects due to small wall-wall separation, capillary waves on the wetting film [63, 64] or the influence of an

external potential. Another interesting point of investigation is the effect of softness of the wall-fluid potential [65].

Chapter 4

Platelets in magnetic and gravitational fields

So far we have investigated hard platelets in bulk, studied the free IN interface and found that the nematic phase wets a hard wall, which can be viewed as an external field with infinite field strength. In the current chapter, we will investigate hard platelets under the influence of finite external fields. In section 4.1 we study the influence of a magnetic field, while in section 4.2 the effect of a gravitational field is investigated. Section 4.3 deals with the simultaneous presence of a magnetic and a gravitational field. This is motivated by recent experiments on gibbsite platelets [66]

4.1 Influence of a magnetic field on the isotropic-nematic phase transition

That external fields have an influence on the physical properties of matter is at least known since the work of Kerr [67]: the electro-optical Kerr effect describes the birefringence of materials in strong electric fields. This effect is strongly pronounced in liquids as well as in crystals and is due to a re-alignment of charge carriers in the medium to the external field. However, effects due to electric and / or magnetic fields are not restricted to specific materials. For suspended nonspherical colloidal particles, the electric and diamagnetic susceptibility will in general differ along the different axes of the particles. This dielectric or diamagnetic anisotropy causes an interaction between the colloids and the external field. As we will show below in detail, the magnetic energy depends on the angle between the external field and the particle symmetry axis. From this fact it is intuitively clear that a magnetic

and / or electric field will have an influence on the orientational distribution of such nonspherical colloids. This may not only change the location of liquid crystal phase transitions like the IN transition for example, but also lead to effects in the isotropic phase, e.g. field induced birefringence, which can be measured in experiments using polarised light [15, 68]. Refs. [69, 70] report investigations of the physical properties of goethite nanorods. The authors observe an alignment of the rods parallel to the direction of a magnetic field for small field strengths and perpendicular to the field for large field strengths both in the isotropic and in the nematic phase. Alignment of particles to an external field was also observed for suspensions of *fd*-viruses, which are rod-like in shape [71,72]. The necessary field strength to observe a certain degree of alignment is higher than in the case of the goethite nanorods due to the lower diamagnetic anisotropy of the *fd*-viruses. For platelike particles, a magnetic field-induced effect was found in [73,74]. Ref. [73] investigates the nucleation mode of platelets of uniaxial ferromagnets in arbitrarily oriented external magnetic fields. In Ref. [74], the authors consider ageing single crystals of Fe-N alloy at various temperatures in external magnetic fields. They find orienting effects which they attribute to the interplay between the magnetisation of an iron matrix and the anisotropic magnetisation.

The field-induced alignment of the particles leads to preordering in the "isotropic" phase; the phase is *paranematic* rather than isotropic. A relevant question is what effect this preordering has on the IN transition. This was investigated within the Onsager theory for thin hard rods in Ref. [75]. The authors find that above a certain strength of the external field the first-order IN transition vanishes in a critical point. An extension to thick rods was given in Ref. [76] using the Parsons-Lee functional [77–79]. Here, a dependence of the critical field strength on the width to length ratio of the rods was found. Ref. [80] is about the phase behaviour of hard rods in an orienting external field. In Ref. [81] the authors calculate the phase coexistence curve for rods and platelets for a negative anisotropic polarizability (susceptibility) on the basis of Onsager theory and find a tricritical point. As can be expected from the difficulties to describe the IN transition of platelets in bulk quantitatively correct, this is only qualitatively correct in the case of platelets.

Here we consider a system of hard platelets under the influence of an external magnetic field. The orientation of the platelet is denoted by the angle θ between the platelet orientation $\boldsymbol{\omega}$, as introduced in chapter 2, see Fig. 2.1. Additionally, we assume a magnetic field pointing along the z-direction. The induced magnetisation $\mathbf{m}$ in the coordinate system spanned by the platelet orientation $\boldsymbol{\omega}$ and $\mathbf{e}_\perp$ (see Fig. 4.1), is given by

$$\mathbf{m} = \chi_m \mathbf{H}, \tag{4.1}$$

where χ_m is the magnetic susceptibility and $\mathbf{H}$ is the magnetic field strength. With $\mathbf{H} = \mathbf{B} - 4\pi\mathbf{M}$ with $\mathbf{B}$ being the magnetic induction we find

$$\mathbf{m} = \frac{\chi_m}{1 + 4\pi\chi_m}\mathbf{B} \approx \chi_m\mathbf{B} \quad (\text{for} \quad |\chi_m| \ll 1). \tag{4.2}$$

In the following we will refer to $\mathbf{B}$ as the magnetic field. Due to the fact that χ_m differs along the different axis of the platelet, we write

$$\mathbf{m} = \chi_\parallel B_\parallel \boldsymbol{\omega} + \chi_\perp B_\perp \mathbf{e}_\perp, \tag{4.3}$$

and the magnetic energy per particle is given by

$$U_{magn} = -\frac{1}{2}\mathbf{m} \cdot \mathbf{B}. \tag{4.4}$$

With $\mathbf{B} = \boldsymbol{\omega} B_\parallel + \mathbf{e}_\perp B_\perp$ this yields

$$\begin{aligned} U_{\text{magn}} &= -\frac{1}{2}\mathbf{m} \cdot \mathbf{B} \\ &= -\frac{1}{2}\left(\chi_\parallel B_\parallel^2 + \chi_\perp B_\perp^2\right) \\ &= -\frac{1}{2}\left(\chi_\parallel \cos^2\theta\, \mathrm{B}^2 + \chi_\perp(1 - \cos^2\theta)\mathrm{B}^2\right) \\ &= -\frac{1}{2}\left((\chi_\parallel - \chi_\perp)B^2\cos^2\theta\right) - \frac{1}{2}\chi_\perp B^2. \end{aligned} \tag{4.5}$$

We next define $\Delta\chi$ as

$$\Delta\chi \equiv \chi_\parallel - \chi_\perp, \tag{4.6}$$

so that we can rewrite (4.5) as

$$U_{\text{magn}} = -\frac{1}{2}\Delta\chi B^2\cos^2\theta, \tag{4.7}$$

where the non-orientation dependent term was neglected. Thus, U_{magn} is a function of the angle θ between the platelet orientation and the z-axis. The platelets in any case favor the alignment that costs the lowest magnetic energy. If $\Delta\chi$ is positive, the platelets will hence align with their normals parallel to the field, a negative value of $\Delta\chi$ leads to a perpendicular alignment. Recall that at the (bulk) IN transition symmetry breaking takes place. In the isotropic phase, no preferred symmetry axis exists while in the nematic phase the platelets are oriented preferentially along the nematic director. Applying planar geometry, this is chosen to be the z-axis, and the phase is uniaxial because of invariance under rotation around the z-axis. In a magnetic field with positive $\Delta\chi$, where parallel alignment to the field is observed,

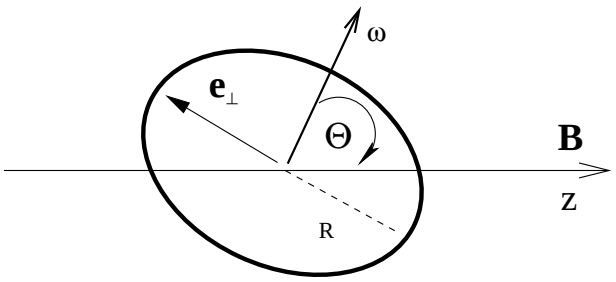

Figure 4.1: Hard platelet with a magnetic field **B** orientated parallel to the z-axis. R is the radius of the platelet, $\boldsymbol{\omega}$ denotes the platelet orientation and θ is the angle between $\boldsymbol{\omega}$ and the z-axis. $\mathbf{e}_\perp$ is a unit vector perpendicular to $\boldsymbol{\omega}$.

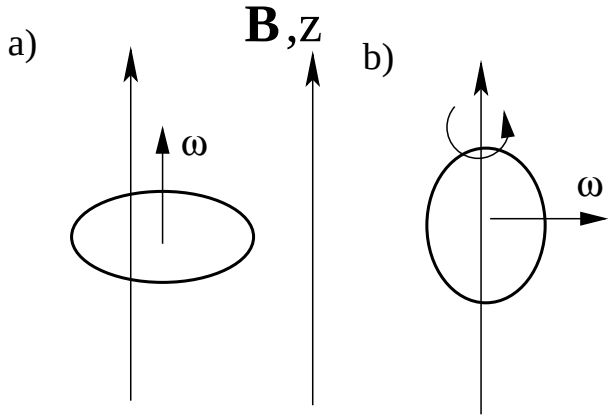

Figure 4.2: Typical orientations of hard platelets in a magnetic field **B**, with orientation of the nematic director (a) parallel and (b) perpendicular to the field direction. In (a), the symmetry is uniaxial, in (b) biaxial.

the nematic phase remains uniaxial, see Fig. 4.2a. For negative $\Delta\chi$ and perpendicular alignment the nematic phase will become biaxial due to rotations of the platelet around the direction of **B**, see Fig. 4.2b.

We next discuss the case with $\mathbf{B} \perp z$ and $\Delta\chi < 0$ and hence $\boldsymbol{\omega} \perp \mathbf{B}$ (corresponding to Fig. 4.2b). To avoid the biaxiality occurring in this case, one could let the magnetic field **B** rotate around an axis parallel to the z-axis with a periodic time smaller than the relaxation time of the platelets [68]. The platelets would then have to align parallel to the z-axis to be perpendicular

to $\mathbf{B}$ at any time.

Our numerical implementation of the FMT functional in planar geometry cannot describe biaxiality, so we restrict ourselves to cases of uniaxial symmetry. In planar geometry uniaxial symmetry means that the platelets in the nematic phase preferentially orient with their normal parallel to the z-axis and hence the order parameter $S > 0$. Thus, we can describe the above discussed situation with a magnetic field $\mathbf{B}$ rotating around an axis parallel to the z-axis. Alternatively we could treat the situation of $\Delta\chi > 0$ and $\mathbf{B} \parallel z$.

We define $V_0 = -(1/2)\Delta\chi B^2$ and use an external potential acting on the platelets given by

$$V_{\text{ext}}(\theta) = V_0 \sin^2(\theta). \tag{4.8}$$

This $\sin^2(\theta)$ dependence is reached with an orientation of $\mathbf{B}$ perpendicular to the z-axis and the rotation of $\mathbf{B}$ around the z-axis, as described above. We have investigated $V_0/k_BT < 0.01$, which corresponds at a temperature $T \approx 300K$ to a value of $\Delta\chi \approx -1 \cdot 10^{-22} J/T^2$ and a magnetic field strength of $B < 8T$. Due to the rotation of the field the effective field strength is only $4T$. The results for density ρ and order parameter S at the IN transition are shown in Fig. 4.3. Fig. 4.3a shows the variation of the paranematic and nematic coexistence densities (horizontal axis) as a function of the field parameter V_0 (vertical axis). The transition is shifted to lower densities, whereby the density jump decreases slightly with increasing field strength. Further increasing V_0/k_BT, the density jump becomes significantly smaller. Above a value $V_0 = 0.02k_BT$ the isotropic coexistence density starts to *increase* again, while the nematic coexistence density continues to decrease. The binodal ends in a critical point at $\rho = 0.423$ and $V_0 = 0.045$. For larger values of V_0/k_BT, there is no phase transition observable anymore. The chemical potential at coexistence, which we plot in the inset of Fig. 4.3a, decreases monotonically and almost linearly with V_0. In Fig. 4.3b we plot the value of the order parameter S at coexistence in the paranematic and nematic phases. We observe $S > 0$ in the paranematic phase due to the influence of the magnetic field, so the term "paranematic" is correct. The value of S in the paranematic phase at coexistence increases monotonically with increasing field strength, while the value in the nematic phase decreases. We attribute this to the shift of the IN-transition to lower densities which are connected with a lower order parameter, see Fig. 3.1a. Remarkably this effect overcompensates the ordering effect caused by the external field.

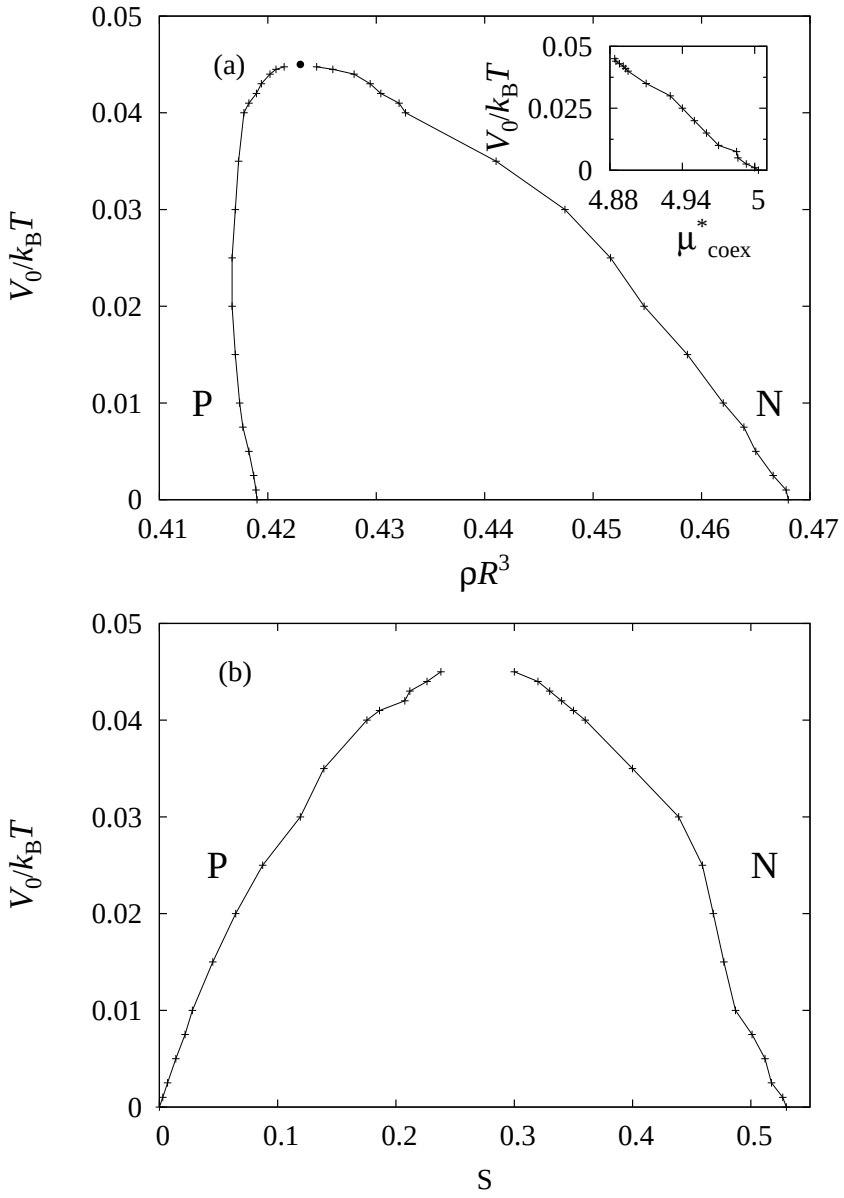

Figure 4.3: a) Isotropic (left graph) and nematic (right graph) coexistence densities (horizontal axis) and the field parameter V_0/k_BT (vertical axis). P and N denote the paranematic and nematic phases, respectively. The critical point at $\rho = 0.423$ and $V_0 = 0.045$ is indicated by the closed circle. b) Same as a), but for the order parameter S in the isotropic and nematic phase. The inset shows the chemical potential μ^*_{coex} as a function of the field parameter V_0/k_BT.

4.2 Sedimentation of hard platelets

Gravity acting on colloidal suspensions leads to sedimentation of the colloidal particles. The first investigation was done by Perrin [82] in 1910. The sedimentation profiles can be used to get information about the equation of state, $P(\rho)$ [83]. For platelets, this was done by simulations in Ref. [60]. Sedimentation profiles of charged colloids are investigated in [84]. Ref. [85] investigates gravity induced liquid crystal phase transitions of colloidal platelets with MC-simulations.

DFT has been used as an ideal tool to treat the influence of gravity on colloidal suspensions: Ref. [86] investigates the competition between sedimentation and phase coexistence of binary systems under gravity. Ref. [87] uses DFT and computer simulations to investigate sedimentation equilibria of colloid-polymer mixtures within the Asakura-Osawa-Vrij model. Ref. [88] is about the colloidal brazil-nut effect in charged binary colloidal suspensions and investigates this effect by DFT and computer simulations. The authors find that heavy colloidal particles sediment on the top of the lighter ones, provided that their mass per charge is smaller than that of the lighter ones.

The strength of gravity can be quantified by the gravitational length ξ_g, defined as

$$\xi_g = k_B T/mg, \tag{4.9}$$

where g is the gravitational acceleration and m is the buoyancy mass of one particle. We consider the case of a fixed total number of particles in the system. This accords to usual experimental conditions. The total number of particles per unit area A in a system of length L is obtained from the density profiles as

$$\frac{N}{A} = \int_0^L dz\, \rho(z). \tag{4.10}$$

In order to obtain density profiles $\rho(z)$, we start with the grand potential, which reads

$$\begin{aligned}\beta\tilde{\Omega}([\rho]) = &\int_0^L dz \int d\theta \rho(z,\theta) \left(\ln(\rho(z,\theta)\Lambda^3) - 1\right) + \beta F_{\text{exc}}[\rho(z,\theta)] \\ &+ \beta \int_0^L dz \int d\theta \rho(z,\theta)[V_{\text{ext}}(z,\theta) - \mu].\end{aligned} \tag{4.11}$$

In the case of an ideal gas, $F_{\text{exc}}[\rho] = 0$, we find after the minimisation proce-

dure given in Eq. (2.2) the well known barometric law,

$$\rho(z) \sim \exp(-z/\xi_g). \tag{4.12}$$

For a gravitational field the external potential is given by

$$V_{\text{ext}}(z) = mgz. \tag{4.13}$$

Thus, V_{ext} depends only on z, and we can define a z-dependent function $u(z)$ as

$$u(z) := V_{\text{ext}}(z) - \mu = [mgz - \mu]. \tag{4.14}$$

$u(z)$ can be viewed as a *local* chemical potential, which serves as an input quantity to the (z-dependent) FMT. The FMT includes nonlocal correlations as can be seen by the occurrence of convolutions in the weighted densities (see subsection 2.3.1). The z-independent part μ of the local chemical potential is a free parameter which we use to ensure $N/A = \text{const.}$ for different values of R/ξ_g. N/A can be obtained from the density profiles via Eq. (4.10).

We display the results of our calculations in Fig. 4.4. One hard wall is located at $z = 0$, a second wall is situated at $z = 100R$. Fig. 4.4a shows the density profile $\rho(z)$ as a function of the height z/R. Plotted are results for different values of the field strength R/ξ_g for $N/A = \text{const}$. We find that the density at the bottom of the system increases with increasing values of R/ξ_g, whereas the density in the upper regions decreases. This can be explained with the fact that increasing R/ξ_g means that the buoyancy mass m has to increase. This leads to an accumulation of particles at the bottom and due to the constraint $N/A = \text{const}$ to a decreasing number of particles in the upper regions. In Fig. 4.4b we plot the results for the local order parameter $S(z)$. In agreement with the observed increase of the density we find increasing values of $S(z)$ at the bottom for increasing R/ξ_g. The decrease of $S(z)$ in the upper region is weaker than for $\rho(z)$. This might be explained by the already low absolute value of $S(z)$ in the upper part already for $R/\xi_g = 0.01$.

4.3 Sedimentation of hard platelets in a magnetic field

The effects of simultaneous presence of a magnetic and gravitational field have been investigated in Refs. [89, 90]. Ref [89] studies experimentally the microstructure of magnetite colloids exposed to a magnetic field, and Ref. [90] is about the preparation and sedimentation behaviour of magnetite-covered

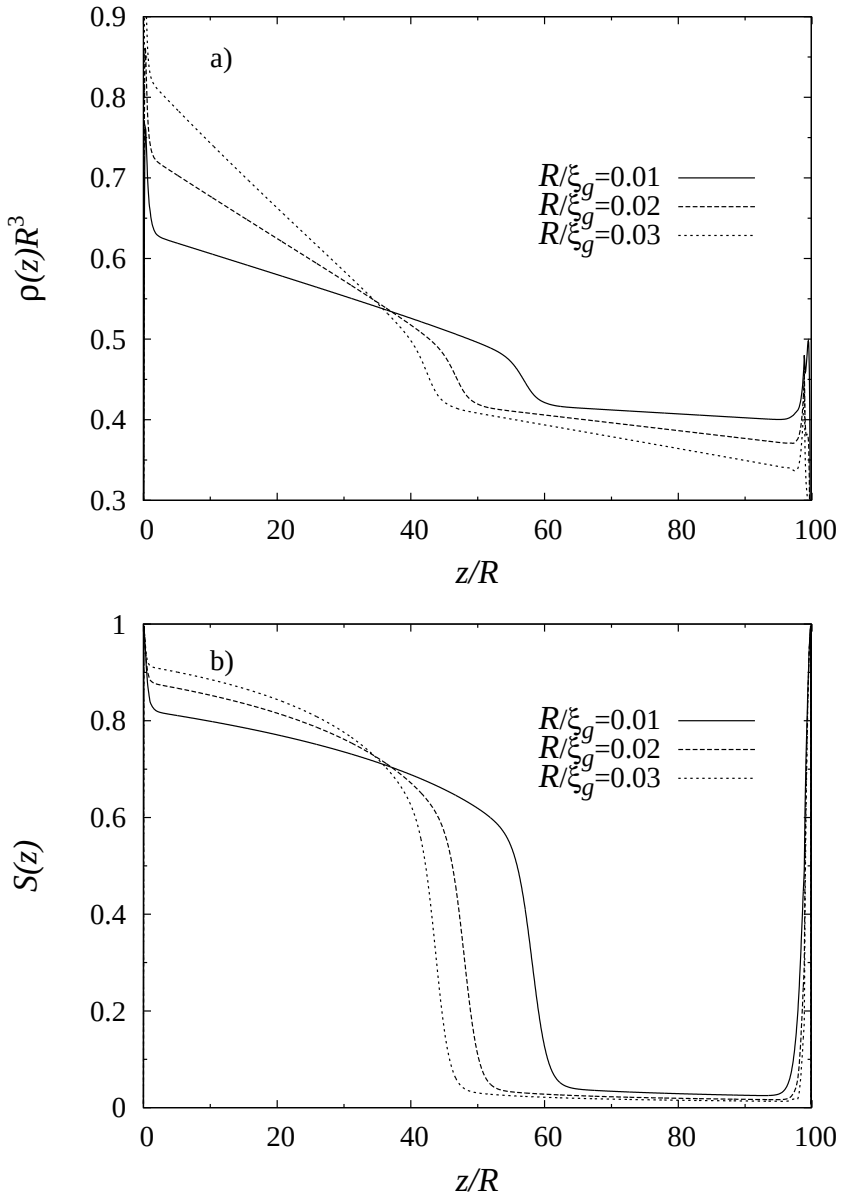

Figure 4.4: a) Density profile $\rho(z)$ as a function of the distance from the wall at $z = 0$ from z-dependent FMT for different values of the inverse gravitational length R/ξ_g. A second wall is located at $z = L = 100R$ with the system length L. b) Same as a), but for the order parameter profile $S(z)$.

clay particles. The authors study the sedimentation behaviour in absence or presence of an external magnetic field.

We next consider a magnetic field (as described in section 4.1) in addition to gravity. Again we assume that the magnetic field rotates around the z-axis to avoid biaxiality as discussed above, see Fig. 4.5 for a sketch of the system. In experiment, the rotation has the function to anneal the sample additionally to orienting the particles. A further effect is a rid of defects within the sample due to the rotation. We will treat this system with two different approaches, i) a local density approximation DFT (LDA) and ii) the full z-dependent FMT used in the previous sections. In the LDA, we solve the (bulk) Euler-Lagrange equations for each height z of the system with the local chemical $u(z)$. Thus, LDA is not able to describe for example hard wall effects correctly and is appropriate only for cases where slowly varying density profiles can be expected. We compare the LDA results with those obtained from the full z-dependent FMT. For a constant gravitational field

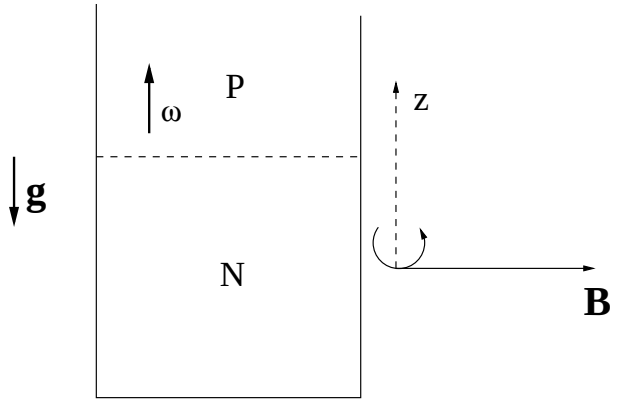

Figure 4.5: Probe with hard platelet fluid, paranematic (P) in the upper part, nematic (N) in the lower part. The magnetic field **B** is rotating around the z-axis to avoid biaxial ordering of the platelets.

and a magnetic field which depends only on the angle θ between the platelet normal and the magnetic field, the external potential V_{ext} is given by

$$V_{\text{ext}}(z,\theta) = -(1/2)\Delta\chi B^2 \sin^2(\theta) + mgz. \tag{4.15}$$

With the abbreviation $V_0 = -(1/2)\Delta\chi B^2$ we can write

$$V_{\text{ext}}(z,\theta) - \mu = V_0 \sin^2(\theta) + [mgz - \mu]\,. \tag{4.16}$$

Thus, V_{ext} is the sum of a θ-dependent part $V_0 \sin^2(\theta)$ and a z-dependent part $u(z) = [mgz - \mu]$. In the LDA we solve the bulk Euler-Lagrange equations

for $u(z)$ independently at each height z of the system. The z-dependent FMT takes the function $u(z)$ as an input quantity and includes nonlocal correlations as discussed in the previous section. In both cases the chemical potential μ is a free parameter which has to be chosen to ensure $N = \text{const}$ for different values of V_0. N is again obtained from the density profiles via Eq. (4.10).

The density profiles from LDA are shown in Fig. 4.6. Plotted is the density profile $\rho(z)$ against the scaled height z/ξ_g. In Fig. 4.6a the profiles are plotted for fixed scaled chemical potential μ^* for a range of values of V_0/k_BT. In this case, the total number of particles N/A increases with increasing V_0/k_BT due to the aligning effect of the magnetic field. Fig. 4.6b shows the density profiles $\rho(z)$ against the scaled system length z/L for $L/\xi_g = 1$. The chemical potential μ^* for a given value of V_0 is chosen to ensure $N/A = \text{const.}$ for all values of V_0. Surprisingly we find that the density for larger values of V_0 decreases at the bottom of the system, $z/L < 0.5$. We attribute this to preordering effects in the paranematic phase and subsequently increasing density in the upper part of the system. Due to the constant total number of particles, the density has to decrease at the bottom of the system. The order parameter profiles $S(z)$ are plotted in Fig. 4.7a and b. Fig. 4.7a shows the profiles for the same fixed chemical potential μ^* as in Fig. 4.6a. We find an increasing nematic order in the paranematic phase with increasing magnetic field strength. In Fig. 4.7b the order parameter profiles for a constant total number of particles are plotted. The value of the order parameter at the bottom of the system remains nearly constant upon increasing the field strength. This might be explained with the decreasing density found at the bottom discussed above (see Fig. 4.6b) and hence decreasing nematic order Finally, we show the product $\rho(z)S(z)$. This product is interesting because it is proportional to the retardation of polarised light which is sent through a tube with colloidal platelets. Thus, it can be measured experimentally [68] and could enable an experimental test of our results. $\rho(z)S(z)$ becomes lower at the bottom of the system for increasing field strength, as would be expected from the behaviour of $\rho(z)$ and $S(z)$. Fig. 4.9 shows the results from the full z-dependent FMT calculation. Here we use z/R as a scaled height coordinate. The field strength is measured by R/ξ_g, which is fixed to $R/\xi_g = 0.01$. Again, a hard wall is located at $z/R = 0$ and $z/R = 100$. The chemical potential μ^* is chosen to ensure $N/A = \text{const}$ for all values of V_0.

Comparing the results from LDA and FMT, one finds remarkable differences. Within the z-dependent FMT we find ordering effects at both hard walls and density oscillations at the upper wall, see Fig. 4.9a. In contrast to this, the LDA profiles are monotonic. This could be expected due to the

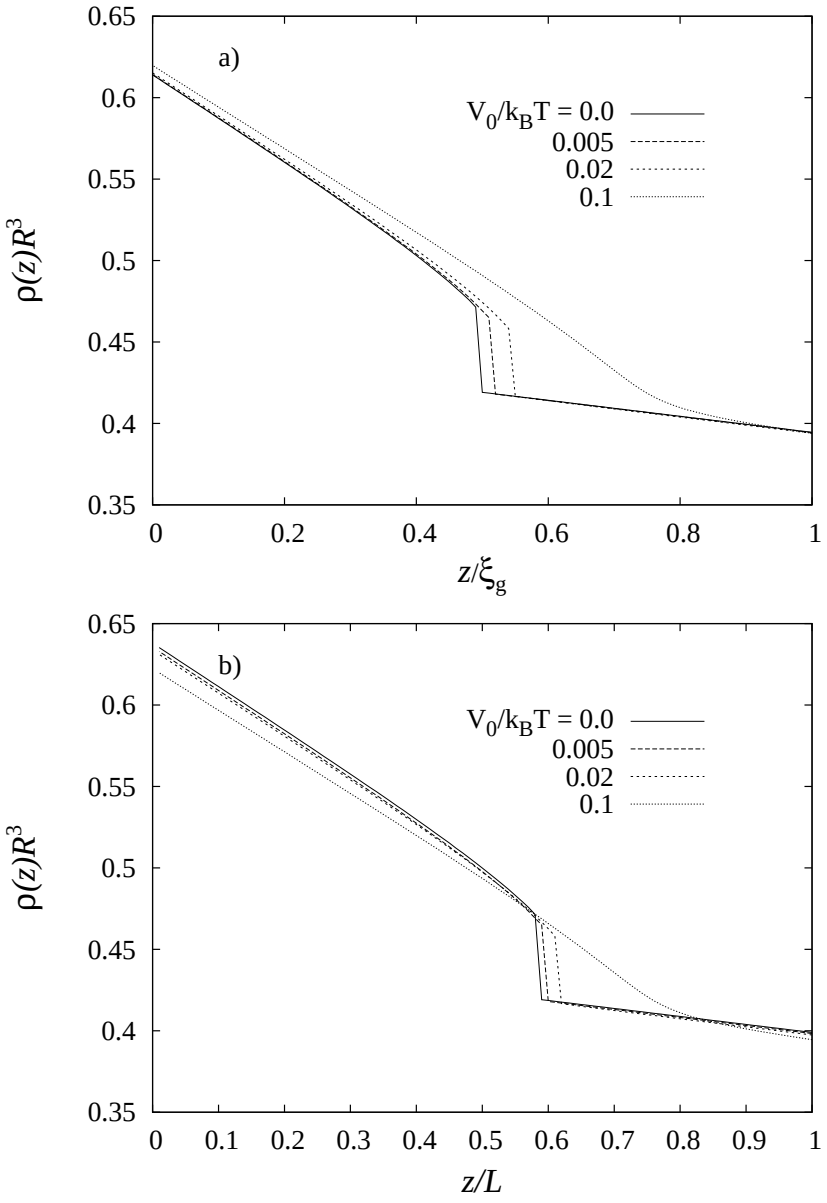

Figure 4.6: a) Density profile $\rho(z)$ as a function of the scaled height z/ξ_g from LDA for different field parameters V_0. b) same as a), but for height scaled with the system length L for different field parameters V_0. Here, the chemical potential μ^* is chosen to ensure $N = \text{const}$ for all values of V_0.

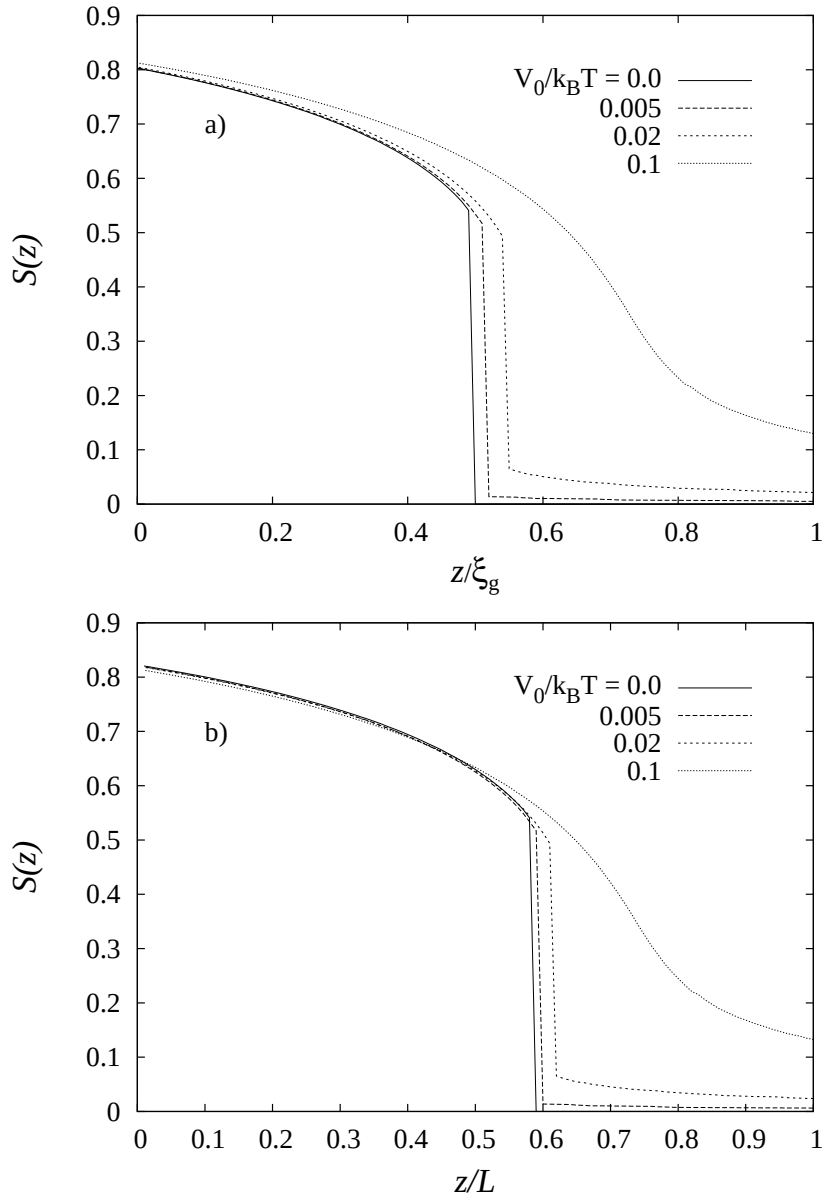

Figure 4.7: a) Same as Fig. 4.6a, but for the order parameter profile $S(z)$ from LDA for different field parameters V_0. b) Same as Fig. 4.6b for the order parameter profile $S(z)$, from LDA.

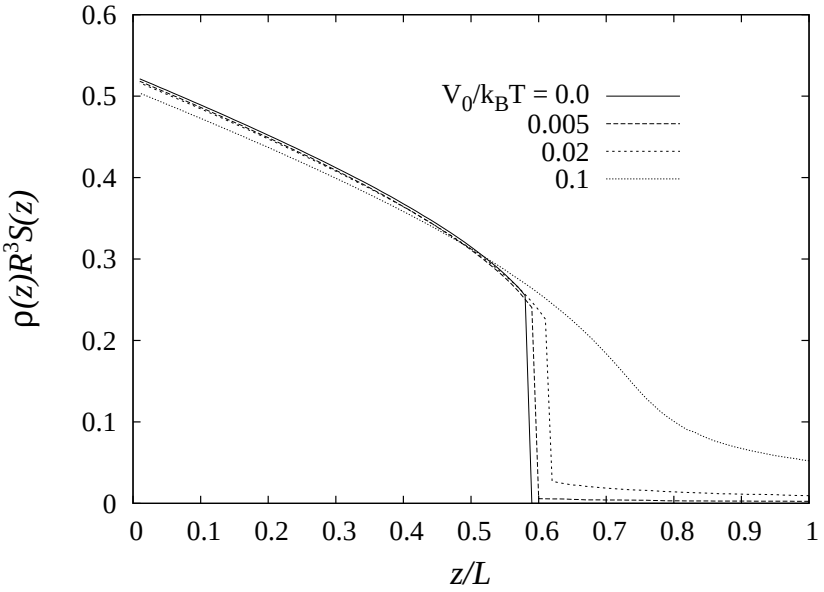

Figure 4.8: Product of density profile and order parameter profile, $\rho(z)S(z)$ from LDA as a function of the height scaled with the system length L.

fact that LDA is a local theory which treats each height z of the system independently from each other. This also explains why the LDA results show a discontinuous jump for the density and order parameter below the critical value of V_0, while the nonlocal FMT obtains a continuous crossover from the isotropic to the nematic phase. Nevertheless the LDA-DFT describes the unexpected properties like the decrease of density at the bottom with increasing field strength correctly.

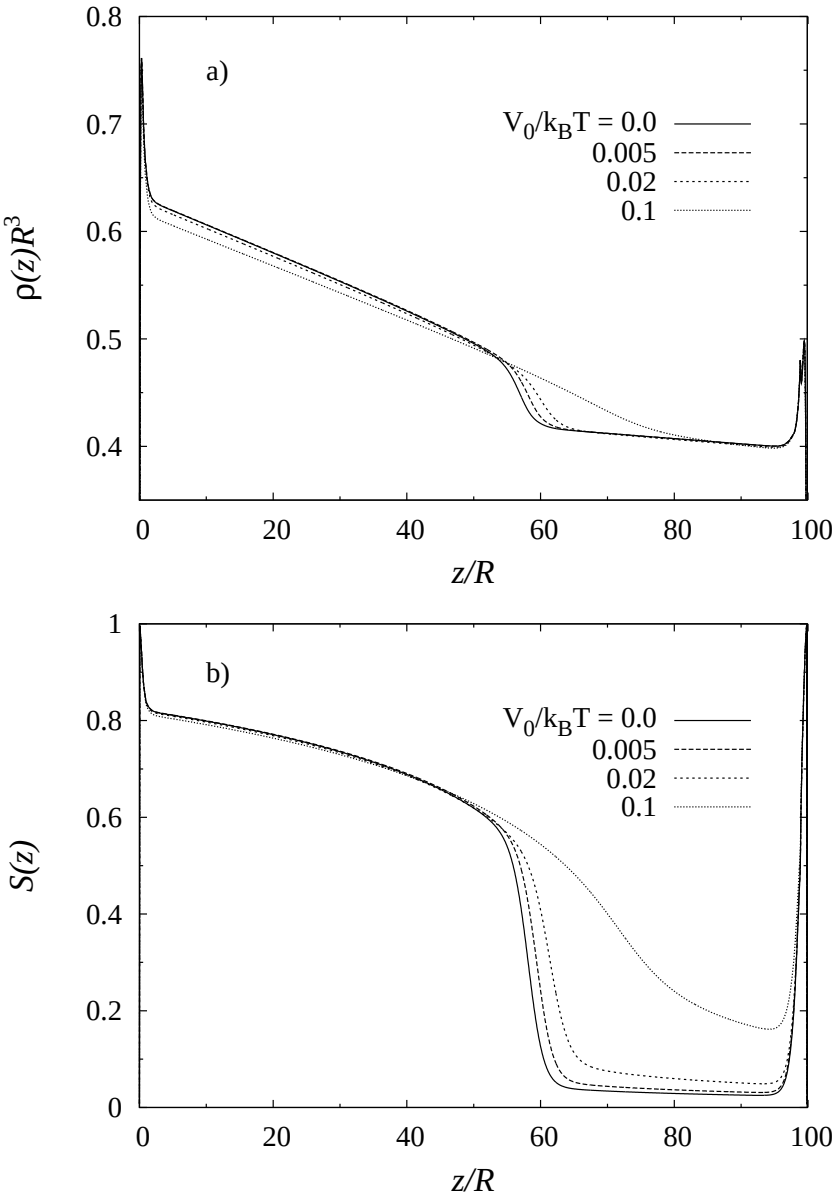

Figure 4.9: a) Density profile $\rho(z)$ as a function of the distance from the wall at $z = 0$ from z-dependent FMT for different values of the field parameter V_0. A second wall is located at $z = L = 100R$ with the system length L. The inverse gravitational length is fixed to $R/\xi_g = 0.01$. b) Same as a), but for the order parameter profile $S(z)$.

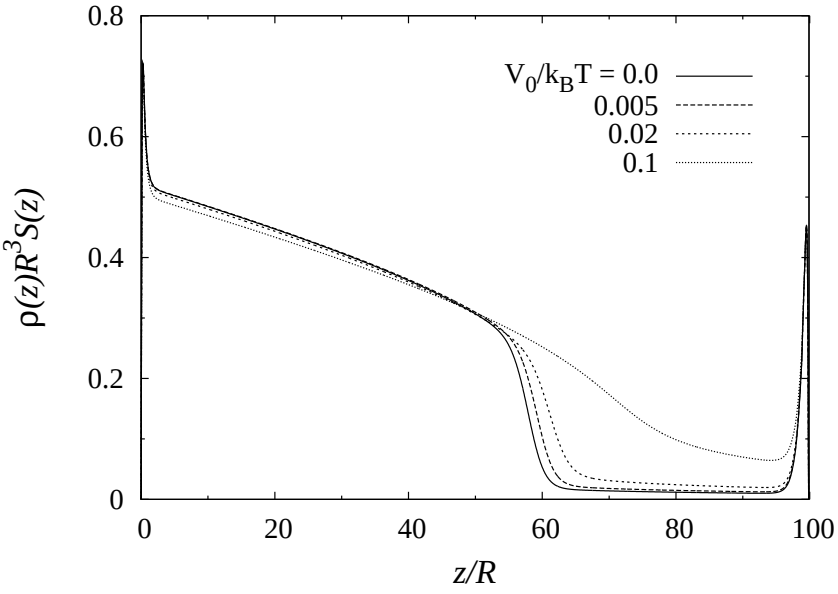

Figure 4.10: Product of density profile and order parameter, $\rho(z) \cdot S(z)$, from FMT for different values of the field parameter V_0. Walls are located at $z = 0$ and $z = L$.

Chapter 5

Capillary nematization of hard platelets

In section 3, we investigated a system of (infinitely thin) hard platelets adsorbed against a single planar hard wall. Due to the complete wetting scenario with thick wetting films, new effects can be expected when two parallel walls are considered and moved close together. In section 5.1 we give an introduction to relevant phenomena occurring in strong geometrical confinement. We investigate these effects for a system of infinitely thin hard platelets in section 5.2. We compare our findings with those for infinitely thin rods between hard walls.

5.1 Introduction

Situations with strong geometric confinement have been considered for different types of liquid crystals and of colloidal particles using theory, simulation and experiments. Capillary condensation was found for simple liquids [91,92] and capillary nematization for thermotropic liquid crystals [93, 94]. *Capillary nematization* is characterised by a shift of the IN transition to a lower chemical potential or equivalent lower (bulk) densities. Thus, it represents a similar case to the more general phenomenon of *capillary condensation*, which is the shift of the vapour-liquid transition in a slit or pore. Ref. [95] investigates hard rods confined by two parallel hard walls using integral equations and computer simulations . The authors examine the dependence of the free energy on the separation of the walls and speculate that capillary nematization should occur. Refs. [26,27] find capillary nematization for biaxial hard rods within the Zwanzig model, and Ref. [28] confirms these results

with MC simulations. Ref. [96] investigates a confined soft ellipsoid fluid with DFT, and in ref. [97] computer simulations of long thin hard rods in a quasi-two-dimensional planar geometry are performed. In Refs. [98, 99], a detailed discussion of hard rods in a capillary with walls acting on the centres of the rods and an additional external potential can be found. The authors find capillary nematization as well as *capillary smectization*. The latter describes a shift of the nematic-smectic phase transition to lower chemical potentials upon confining the system. Much less work has been devoted to systems of confined hard platelet fluids. In Ref. [36] the authors investigate the wetting and capillary nematization behaviour of binary hard-platelet and hard-rod fluids using the Zwanzig model. They obtain density profiles and find a capillary critical point upon decreasing the wall separation. Here we treat the same phenomena but for a pure platelet fluid using a model with continuous orientations.

5.2 Results

We next investigate capillary effects for the case of hard platelets. For reasons of comparison, we also treat the case of rods and compare our findings in the following section.

Recall that the free IN interface and the wetting profiles of platelets at a single hard wall decay smoothly to their bulk values, see e.g. Fig. 3.2a and b of chapter 3. The bulk values of density and the order parameter are reached at a distance from the wall of $\approx 10R$. From this fact one can expect that geometrical confinement will have an effect on the phase transition for even large wall-to-wall separations. Our goal is to determine the values of the isotropic and nematic densities, order parameter as well as the chemical potential at coexistence as a function of the wall separation.

The separation between both walls is denoted by H, and the relative capillary width is defined as $h = H/R$, thus bulk corresponds to $h = \infty$. We next define spatial averaged quantities $\langle\rho\rangle$ and $\langle S\rangle$ to compare our results for different values of h,

$$\langle\rho\rangle = \frac{1}{H}\int_0^H dz\,\rho(z), \tag{5.1}$$

and

$$\langle S\rangle = \frac{1}{H}\int_0^H dz\,S(z). \tag{5.2}$$

In Fig. 5.1a we plot the results for the coexistence densities as obtained for platelets. The results for the order parameter follow in Fig. 5.2a. For increasing $1/h$ (and thus decreasing capillary width) we at first observe increasing isotropic and nematic coexistence densities, although the chemical potential μ^* at coexistence is shifted to lower values, see the inset of Fig. 5.1a. This increase of the average density can be explained with the adsorption-layer at the wall which contributes strongly to $\langle\rho\rangle$ for small h. With further increasing $1/h$ the isotropic coexistence density initially continues to increase, but the slope decreases. We attribute this to the shift of the IN transition to lower chemical potentials, which is an effect in the opposite direction to the density increase due to the adsorption layer. The nematic coexistence density has a maximum at $1/h = 0.041$ or $H = 2.44R$ and starts to decrease again beyond this point. The binodal ends in a critical point at $1/h = 0.086$ or $H = 11.6R$. The behaviour of the order parameter $\langle S\rangle$ confirms these results, see Fig. 5.2a. The isotropic coexistence value increases with increasing $1/h$, until the critical point is reached. For the nematic coexistence curve we also find the maximum at $1/h = 0.41$ or $H = 2.44$.

We compare our results for the chemical potential at capillary coexistence with those obtained from the Kelvin equation. The Kelvin equation has been tested for simple fluids in slit pores [91, 92] and for a lattice model of the IN transition [100] and is given by

$$\Delta\mu = \frac{2\gamma_{IN}R^2}{h(\rho_N - \rho_I)}, \tag{5.3}$$

where $\Delta\mu = \mu_{\text{coex}}^{\text{bulk}} - \mu_{\text{coex}}^{\text{cap}}$ is the change of the chemical potential at coexistence due to the capillary of width h, and γ_{IN} is the IN interfacial tension for complete wetting. With the value $\gamma_{IN}R^2/k_BT = 0.006656$ obtained in chapter 3 and $\rho_N R^3 - \rho_I R^3 = 0.05$ we can calculate $\Delta\mu$ as a function of h. The results are plotted in the inset of Fig. 5.1a. The predictions of the Kelvin equation for the capillary coexistence chemical potential are in good agreement with the results from the calculations for $1/h = 0.043$ (which corresponds to a capillary width of $h = 23.1$) but become increasingly poor for larger values of $1/h$. This could be expected as the Kelvin equation is valid only for $h \gg 1$.

In Fig. 5.3a we plot examples of the isotropic and nematic density profiles $\rho(z)$ and order parameter profiles $S(z)$ at coexistence for capillary widths of $h = 23.1, 18.1, 13.0, 12.0$. The density in the middle of the capillary *increases* from $h = 23.1$ to $h = 13$ from $\rho = 0.418$ to $\rho = 0.42$, although the chemical potential at coexistence *decreases*. This can be explained with the fact that for $h = 13$ the wetting films from both walls "see" each other and so shift

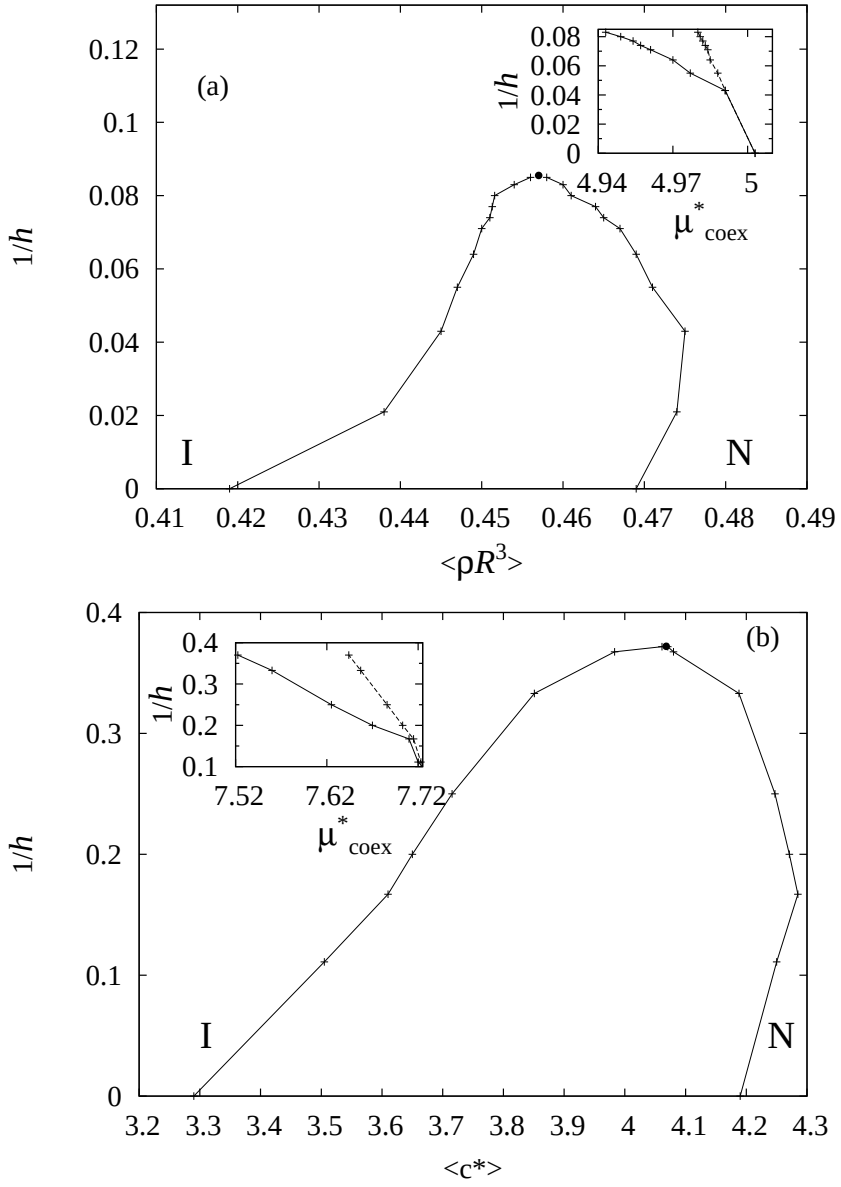

Figure 5.1: a) Variation of the isotropic and nematic coexistence densities (horizontal axis) with the inverse capillary width $1/h$ (vertical axis) as obtained for platelets. The density $\langle\rho\rangle$ is defined via Eq. (5.1). The critical point at $\langle\rho\rangle = 0.457$ and $1/h = 0.086$ is indicated by the closed circle.The inset shows the decrease of the chemical potential $\mu^*_{\rm coex}$ due to the walls as obtained from FMT (full line) and from the Kelvin equation (dotted line). b) Same as a), but as obtained for rods. The density $\langle c*\rangle$ is defined via Eq. (5.5). The critical point at $\langle c^*\rangle = 4.07$ and $1/h = 0.373$ is indicated by the closed circle.

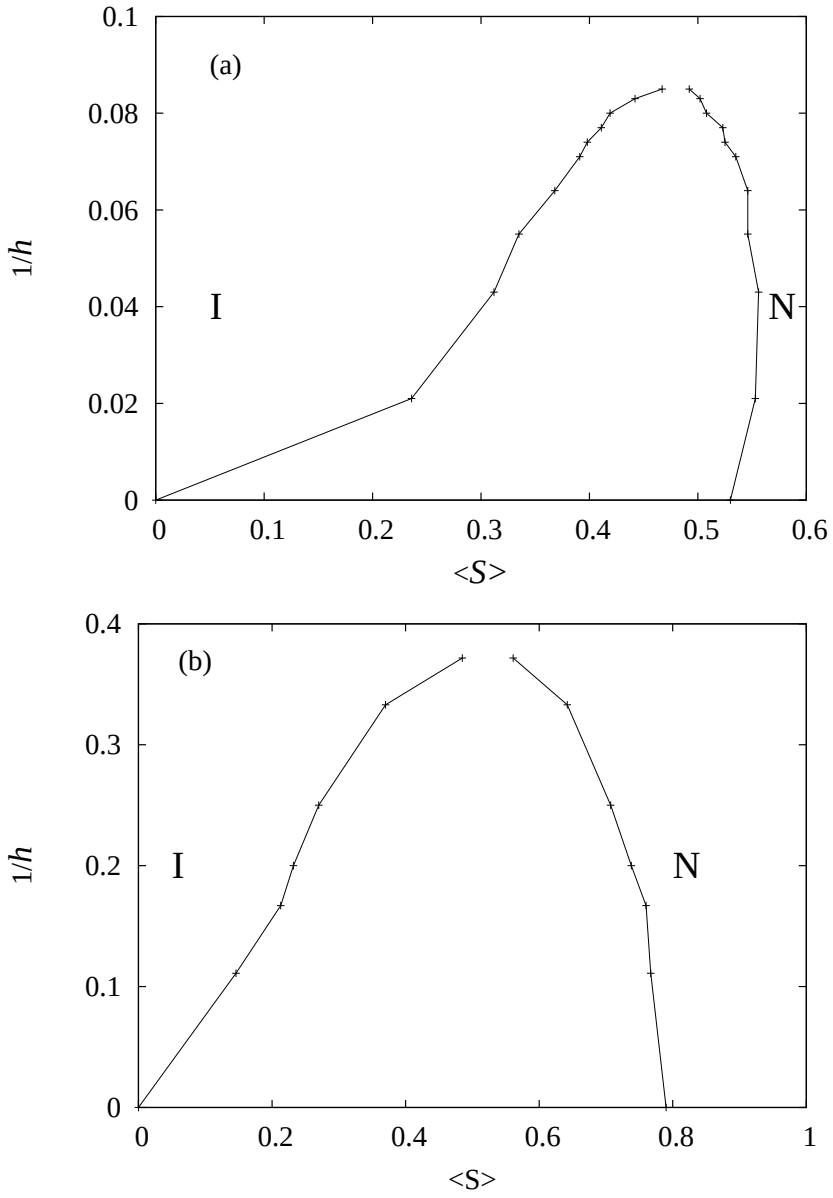

Figure 5.2: a) Variation of the values of the average order parameter $\langle S \rangle$, defined in Eq. (5.2), for the isotropic and . nematic profile (horizontal axis) with the inverse capillary width (vertical axis) as obtained for platelets. b), Same as a), but as obtained for rods. The average order parameter is defined via Eq.(5.6).

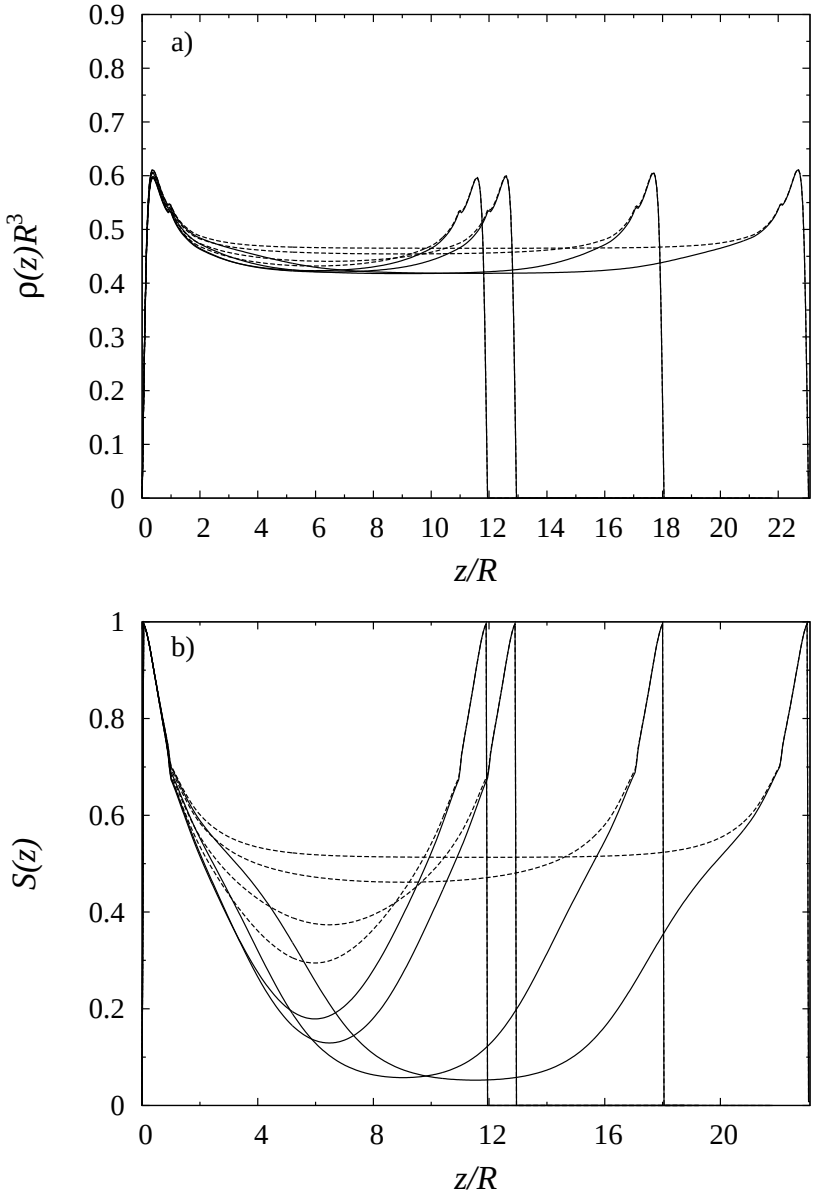

Figure 5.3: a) Density profile $\rho(z)$ as a function of the distance from one of the walls for $h = 23.1, 18.1, 13.0, 12.0$ as obtained for platelets. Plotted are the isotropic (full line) and nematic (dashed line) coexistence profiles. The coexistence chemical potential decreases from $\mu^* = 4.995$ at $h = 23.1$ to $\mu^* = 4.9459$ at $h = 12.0$ b) Same as a), but for order parameter profile $S(z)$.

the density to a higher value. The isotropic and nematic order parameter profiles $S(z)$, which we plot in Fig. 5.3b for the same values of h as the density profiles,, are similar to those from chapter 3 for a single wall, compare Fig. 3.5a. Here however capillary effects are clearly visible for $h = 13$ and $h = 12$, see Fig. 5.3b: the value of the order parameter for the isotropic coexistence profile in the middle of the capillary is with $S > 0.15$ significantly larger than zero. It is even larger than the value of $S = 0.045$ which found with the z-dependent FMT in chapter 3 due to numerical reasons. The nematic profile at the middle of the capillary is with $S = 0.4$ lower than that of the bulk coexistence value, consistent with the shift of the chemical potential to lower values.

We next investigate the capillary behaviour of rods. Although this calculation was already done [98, 99] for a hard wall acting on the centres of the rods with an additional potential, we perform this calculation again to compare the results for platelets and rods as obtained from our FMT functional.

In particular, we compute the isotropic-nematic phase transition in a capillary constituted by two walls acting on the *centre* of the hard rods:

$$V_{ext}(z,\theta) = \begin{cases} \infty & z < 0, z > H \\ 0 & 0 \leq z \leq H \end{cases} \tag{5.4}$$

Due to the fact that the external potential only depends on the spatial coordinate z, the resulting density profiles are uniaxial. Again planar geometry is assumed, where the only spatial coordinate is z and the remaining angle θ is that between the orientation $\boldsymbol{\omega}$ and the z-axis, see Fig. 5.4 for a sketch.

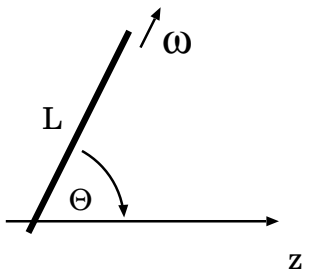

Figure 5.4: Rod with length L, the orientation is denoted by $\boldsymbol{\omega}$, and θ is the angle between $\boldsymbol{\omega}$ and the z-axis.

We next define the dimensionless density c by $c(z,\theta) = \frac{\pi}{4} L^2 D \rho(z,\theta)$ and the orientation-averaged density profile $c^*(z) = \int_0^{\pi/2} d\theta \sin(\theta) c(z,\theta)$. The cap-

illary width is again measured by $h = H/L$, and we define analogously to the platelets the spatial averaged density and order parameter via

$$\langle c^* \rangle = \frac{1}{H} \int_0^H dz\, \rho(z), \tag{5.5}$$

and

$$\langle S \rangle = \frac{1}{H} \int_0^H dz\, S(z). \tag{5.6}$$

Fig. 5.1b and Fig. 5.2b show the results of the calculations. We find the isotropic and nematic coexistence densities to increase with increasing $1/h$. While this increase holds for the isotropic density until the critical point is reached, the nematic density starts to decrease beyond a maximum at $1/h = 0.16$. The binodal ends in a critical point at $1/h = 0.372$. The behaviour of the order parameter $\langle S \rangle$ differs slightly. The isotropic coexistence value decreases monotonically as the density, but the nematic coexistence curve shows no maximum.

Again we apply the Kelvin equation (5.3) to calculate the shift of the chemical potential. The results are plotted in the inset of Fig. 5.1a. We find good agreement with the data obtained from FMT for small $1/h$, for $1/h$ closer to the critical point the predictions become increasingly poor.

Profiles of the density $c(z)$ and the order parameter $S(z)$ for a capillary width of $h = 9, 5, 3$ are plotted in Fig. 5.5 a and b. In the centre of the capillary the bulk values of the density and order parameter are almost reached for $h = 9$ and also $h = 5$. We find the maximum of the density profile $\rho(z)$ directly at the wall, see Fig. 5.5a. In contrast to this, the maximum of the order parameter profile $S(z)$ surprisingly lies *not* directly at the wall, see Fig. 5.5b. When looking at the profiles for $h = 3$, relatively close to the critical point at $h = 2.68$, one finds that the capillary effects are now more pronounced. In the centre of the capillary is the value of the order parameter significantly larger than zero. As observed for $h = 5$ and $h = 9$, the maximum of the density lies at the wall, while the maximum of the order parameter is shifted away from the wall.

For $1/h > 0$ we found that the value of the isotropic order parameter profile is larger than zero in increasing large regions of the capillary. Despite this fact we continued to call this phase "isotropic" because the preordering we find here is different from that in the paranematic phase in section 4.1. There global preordering was found, whereas here we find $\langle S \rangle > 0$ even for

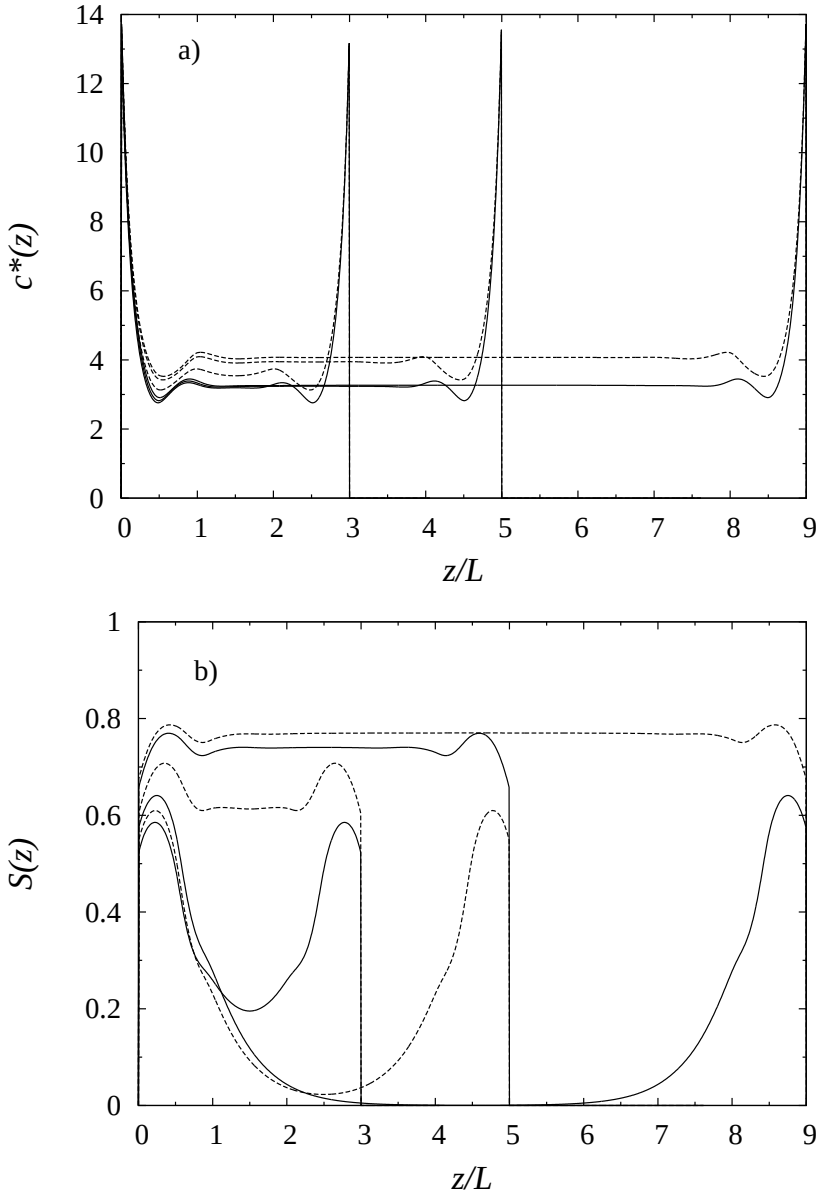

Figure 5.5: a) Density profile $c^*(z)$ as a function of the distance from one of the walls for $h = 9, 5, 3$ as obtained for rods. Plotted are the isotropic (full line) and nematic (dashed line) coexistence profiles. The coexistence chemical potential decreases from $\mu^* = 7.72$ at $h = 9.0$ to $\mu^* = 7.56$ at $h = 3.0$ b) Same as a), but for the order parameter profile $S(z)$.

profiles where still $S(z) = 0$ in the middle of the capillary (see profile for $h = 9.0$ in Fig. 5.5b), which is due to the effect of the adsorption layer.

5.3 Conclusions

Comparing the results found for the capillary nematization of platelets and rods, one finds remarkable differences. The most eye-catching difference is the value of $1/h$ at which the critical point is reached. For platelets, we find it at a capillary width of $H = 11.6R$, for rods at $H = 2.67L$. Because the length L of a rod has to be compared to the diameter D of a plate instead of the radius R, we have to compare $H = 5.8D$ for platelets and $H = 2.67L$ for rods. Thus, the critical capillary width at the critical point for platelets is twice as large as that for rods. We compare this to the correlation lengths which are $\xi_I/D = 0.66$ (at the isotropic side of the free IN interface) and $\xi_N/D = 0.675$ (at the nematic side of the interface) for platelets and $\xi_I/L = 0.335$ and $\xi_N/L = 0.332$ for rods [101]: the correlation length for platelets is about twice the correlation length of the rods. Thus, a larger correlation length leads to a larger capillary width at the critical point, which is intuitively clear from the fact that a larger correlation length means that the wetting profiles from both walls "see" each other at even larger distances.

Comparing $\Delta\mu$ at the critical point, we find $\Delta\mu = 0.25$ for rods and $\Delta\mu = 0.06$ for platelets. Recalling Eq. (5.3), we see that $\Delta\mu$ is proportional to the IN interfacial tension γ_{IN} and inverse proportional to the IN density jump $\rho_I - \rho_N$. The interfacial tension $\gamma_{IN} = 0.006656R^2$ or $\gamma_{IN} = 0.0266D^2$ for platelets is much smaller than that found for rods, which is given by $\gamma_{IN} = 0.16LD$. This is partially compensated by the density jump ($\rho_N - \rho_I = 0.9$ for rods and $\rho_N - \rho_I = 0.05$ for platelets), leading together to a smaller shift for platelets.

Chapter 6

Platelets and rods with finite thickness

So far, we have investigated the behaviour of infinitely thin hard platelets and rods. In nature and hence in experiments, the particles under consideration will have a finite thickness [10–14,68]. For this reason, a theory which is able to predict the phase behaviour of thick anisotropic particles is desirable. In this chapter, we will extend the FMT approaches for rods and platelets used in the previous chapters in order to describe finite thickness. As a test case, we will compute the bulk IN phase transition. In order to do this, we have to add additional contributions to the excess free energy functional. We expect that this is only a first step towards such a theory.

6.1 Introduction

The literature on anisotropic particles with finite thickness is vast. Ref. [102] investigates the phase behaviour of hard rods. The authors use computer simulations and obtain the complete phase diagram for different values of L/D. In Ref. [14,18] the IN transition and the equation of state of cut spheres is computed using MC simulations. Cut spheres are of similar shape as platelets, in particular they are spheres where - symmetric around the equator - spherical caps have been removed. There are several theoretical approaches to treat rods with finite thickness. In Ref. [103], the authors investigate a fluid of perfectly aligned rigid cylinders for radius a and length l with a scaled particle ansatz. A DFT approach is used in Ref. [51] which interpolates between the Rosenfeld [48–50] and the Onsager functional [5]. Results for the IN transition of hard rods and ellipsoids are obtained. The authors conclude

that their results are comparable with those from the Parsons-Lee functional [77–79]. The latter theory is based on a mapping of higher virial coefficients to those of the hard sphere system. Parsons-Lee theory predicts the location of the IN transition accurately for a wide range of shape anisotropies [104, 105], but yields unrealistic density profiles when applied to inhomogeneous situations[]. Other approaches were proposed by Poniewierski and Holyst [106–109] and Somoza and Tarazona [110–112]. In Ref [80] a complex phase diagram of rods is presented, and in Ref. [113] the authors investigate the smectic, nematic and isotropic phases in a mixture of thin and thick hard rods.

6.2 Results for platelets and rods

We now consider platelets with finite thickness. Such a platelet is characterised by the radius R and the thickness L, see Fig. 6.1.

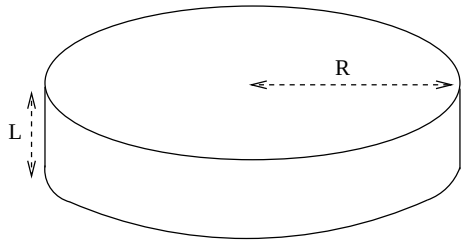

Figure 6.1: A platelet of radius R and thickness L.

To treat thick platelets, we have to modify the expression for the free energy density Φ given in Eq. (2.9), which is suitable for platelets with vanishing thickness. Additional weight functions are required, in particular we need weight functions which describe the volume of a platelet. In Eq. (2.9), this weight function vanishes due to the vanishing thickness. We combine the free energy density given by Eq. (2.9) with the Rosenfeld functional [48–50] and obtain

$$\begin{aligned}\Phi &= \Phi_1 + \Phi_2 + \Phi_3 \\ &= -n_0 \ln(1-n_3) + \frac{n_1^{DD} n_2^D}{1-n_3} + \frac{n_2^D n_2^{DDD} n_2^D}{24\pi(1-n_3)^2},\end{aligned} \tag{6.1}$$

where the additional weighted densities [38] are given by

$$w_0(\mathbf{r},\boldsymbol{\omega}) = \frac{1}{2\pi R}\delta(R-|\mathbf{r}|)\delta(\mathbf{r}\cdot\boldsymbol{\omega}), \tag{6.2}$$

$$w_3(\mathbf{r},\boldsymbol{\omega}) = 2L\Theta(R-|\mathbf{r}|)\delta(\mathbf{r}\cdot\boldsymbol{\omega}). \tag{6.3}$$

w_3 describes the volume of a thick platelet of Radius R and thickness L. w_0 corresponds to the Euler characteristic. The new weighted densities n_0, and n_3 are given by

$$n_0(\mathbf{r},\boldsymbol{\omega}) = w_0(\mathbf{r},\boldsymbol{\omega}) * \rho(\mathbf{r},\boldsymbol{\omega}), \tag{6.4}$$

$$n_3(\mathbf{r}) = \int \frac{d\boldsymbol{\omega}}{4\pi} w_3(\mathbf{r},\boldsymbol{\omega}) * \rho(\mathbf{r},\boldsymbol{\omega}). \tag{6.5}$$

We use the thickness-to-radius ratio L/R as a dimensionless parameter, where $L/R = 0$ corresponds to infinitely thin hard platelets.

In Fig. 6.2 we show results for the equation of state $P(\rho)$ for $L/R = 0.0,\ 0.1,\ 0.2$ in the isotropic phase. The results for $L/R = 0.0$ stem from FMT and for comparison we plot the results from a fifth order virial expansion [6]. The authors compute the virial coefficients up to the fifth order using a diagram technique [114]. For $L/R = 0.1$ and $L/R = 0.2$ we plot results from FMT and a fit function to MC simulation results of cut spheres [19]. We find that FMT overestimates the pressure in the isotropic phase for high densities. The virial expansion as well as the fit parameters contain negative coefficients which lead to a damping of the slope at increasing densities, which is not reproduced by FMT.

In Fig. 6.3 we plot the equation of state $P(\rho)$ in the isotropic and nematic phases for $L/R = 0.0,\ 0.1,\ 0.2$. The results were obtained by FMT and by MC simulations (M. Dijkstra) for $L/R = 0$, see also Fig. 3.1b. For $L/R = 0.1$ and $L/R = 0.2$ we again use the fit function to MC simulations [19]. The isotropic and nematic coexistence densities are indicated by the open and closed circles, respectively. Comparing Fig. 6.3a, b and c, we find that FMT predicts a shift of the IN transition to lower densities, whereby the density jump $\rho_N - \rho_I$ remains nearly constant. The MC simulation results indicate no shift of the IN transition, but predict a decreasing density jump. The pressure in the nematic phase is significantly underestimated by FMT for $L/R > 0$.

In conclusion, the predictions from FMT are not in quantitative agreement with the simulation results for $L/R > 0$. In the isotropic phase, the decrease of the slope of $P(\rho)$ obtained by the MC simulations is not catched

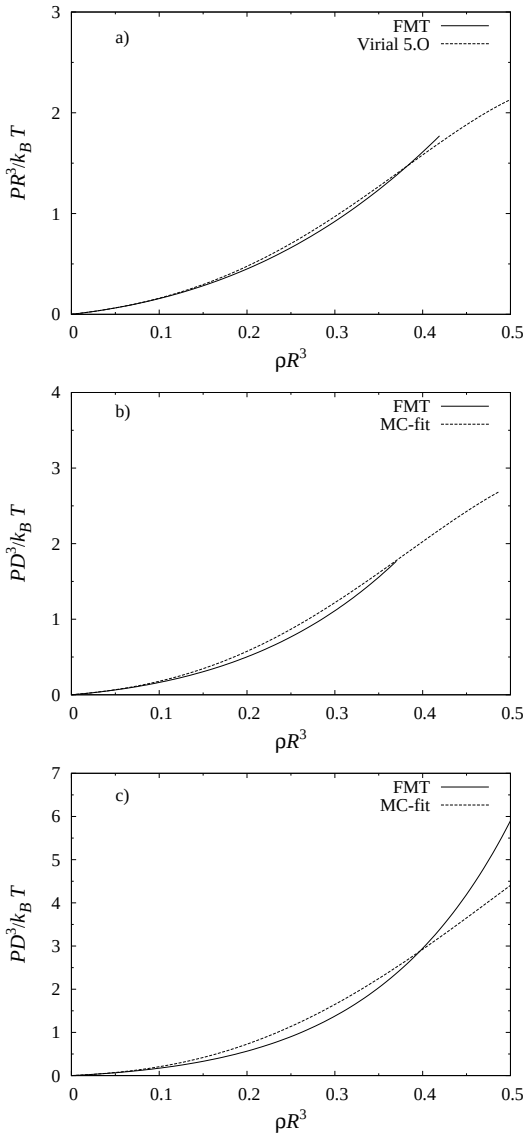

Figure 6.2: a) Equation of state, $P(\rho)$ for $L/R = 0.0$ as obtained from FMT (full line) and a fifth-order virial expansion (dashed line). Shown are results for the isotropic phase. b) same as a), but for $L/R = 0.1$ as obtained from FMT (full line) and a fit function to MC simulations [19] (dashed line). c) same as b) for $L/R = 0.2$.

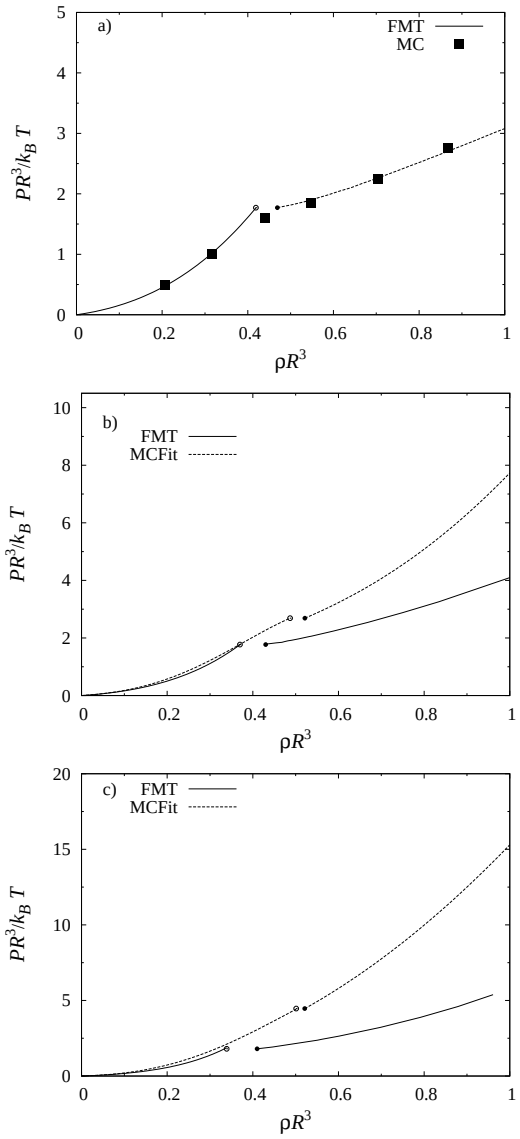

Figure 6.3: a) Equation of state, $P(\rho)$ for $L/R = 0.0$ (a), $L/R = 0.1$ (b) and $L/R = 0.2$ c) as obtained from FMT (full line) and MC simulations by M. Dijkstra (dashed line,a) and a fit function to MC simulations, respectively [19] (dashed line, b and c). Shown are results for the isotropic and nematic phase. The isotropic and nematic coexistence densities are indicated by open and closed circles, respectively.

by FMT, what we explain with the fact that the fit functions to the MC simulations contain negative coefficients, which is not captured by FMT. In the nematic phase, FMT predicts increasing pressure PR^3/k_BT for fixed bulk density ρR^3 as the MC simulations obtain, but significantly underestimates this increase. Also the predictions for the location of the IN transition are not in agreement with those from MC simulations.

We next consider hard rods with finite thickness. In the following, we refer to a rod as to a cylinder of length L, which is capped with two hemispheres of diameter D at the ends, see Fig. 6.4. In literature, the term spherocylinder

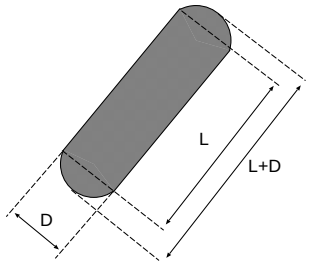

Figure 6.4: A rod (or spherocylinder) of length L and diameter D.

is often used for this kind of thick rods.

As in the case of platelets, we have to modify the free energy density Φ, which is given by Eq. (2.18) for $L/D = 0$. Adding weight functions which describe the volume of the platelet following [48–50], the free energy density is now given by

$$\begin{aligned}\Phi &= \Phi_1 + \Phi_2 + \Phi_3 \\ &= -n_0 \ln(1-n_3) + \frac{n_1 n_2^{NN}}{1-n_3} + \\ &+ \frac{n_2^N n_2^{NNN} n_2^N}{24\pi(1-n_3)^2},\end{aligned} \tag{6.6}$$

with the 3D weight functions w_μ, $\mu = 0, 1, 3$ and w_2^{NN}:

$$w_0(\mathbf{r}, \boldsymbol{\omega}) = \frac{1}{2}(\delta(\mathbf{r} + L\boldsymbol{\omega}/2) + \delta(\mathbf{r} - L\boldsymbol{\omega}/2)), \tag{6.7}$$

$$w_2(\mathbf{r}, \boldsymbol{\omega}) = \pi D \int_{-L/2}^{L/2} dl\, \delta(\mathbf{r} + l\boldsymbol{\omega}), \tag{6.8}$$

$$w_3(\mathbf{r}, \boldsymbol{\omega}) = \frac{\pi D^2}{4} \int_{-L/2}^{L/2} dl \delta(\mathbf{r} + l\boldsymbol{\omega}), \tag{6.9}$$

and the weighted densities n_μ, $\mu = 0, 2$ and n_3:

$$n_\nu(\mathbf{r}, \boldsymbol{\omega}) = w_\nu(\mathbf{r}, \boldsymbol{\omega}) * \rho(\mathbf{r}, \boldsymbol{\omega}) \quad \nu = 0, 2, \tag{6.10}$$

$$n_3(\mathbf{r}) = \int \frac{d\boldsymbol{\omega}}{4\pi} w_3(\mathbf{r}, \boldsymbol{\omega}) * \rho(\mathbf{r}, \boldsymbol{\omega}), \tag{6.11}$$

where L is the length of the cylinder and D the diameter of the hemispheres at the end, see Fig. 6.4. We define the reduced density

$$\rho^* = \rho/\rho_{cp}, \tag{6.12}$$

where

$$\rho_{cp} = 2/(\sqrt{2} + \sqrt{(}3)/(D/L)) \tag{6.13}$$

is the close packing density of hard rods. We performed the calculations with two different approaches, using i) $\Phi_1 + \Phi_2$ and ii) $\Phi_1 + \Phi_2 + \Phi_3$ from Eq. (6.6). We refer to i) as FMT2 and to ii) as FMT3.

Figs. 6.5a,b show the results of the calculations for the isotropic-nematic transition for $D/L = 0.0, 0.05, 0.0667, 0.2$. In Fig. 6.5a we plot the results for the reduced density ρ^* defined above, in Fig. 6.5b for the dimensionless density c^* as defined in section 5.2. The results from FMT2 and FMT3 functionals are in better agreement with the simulation data than the predictions of Onsager theory. The FMT3 functional underestimates the coexistence densities compared to MC results, while the FMT2 functional overestimates them. A different approach with similar results can be found in Ref. [51]. We have to conclude that the FMT3 functional shows no further enhancement when compared to the results from FMT2. This is a kind of surprising, because the truncation of Eq. (6.6) after the Φ_2 term is a bit artificial.

6.3 Conclusion

Our approach to treat finite thickness does not yield satisfying results for the platelets nor for rods. We find in the case of platelets the correct tendency for the equation of state, but the increase of the pressure due to the thickness is underestimated. Also the prediction of the location of the IN transition is not in agreement with the simulations. For rods, this prediction is in slightly better agreement with the simulation results than for platelets, but still not perfect. We conclude that a more profound modification of FMT is necessary to treat finite thickness.

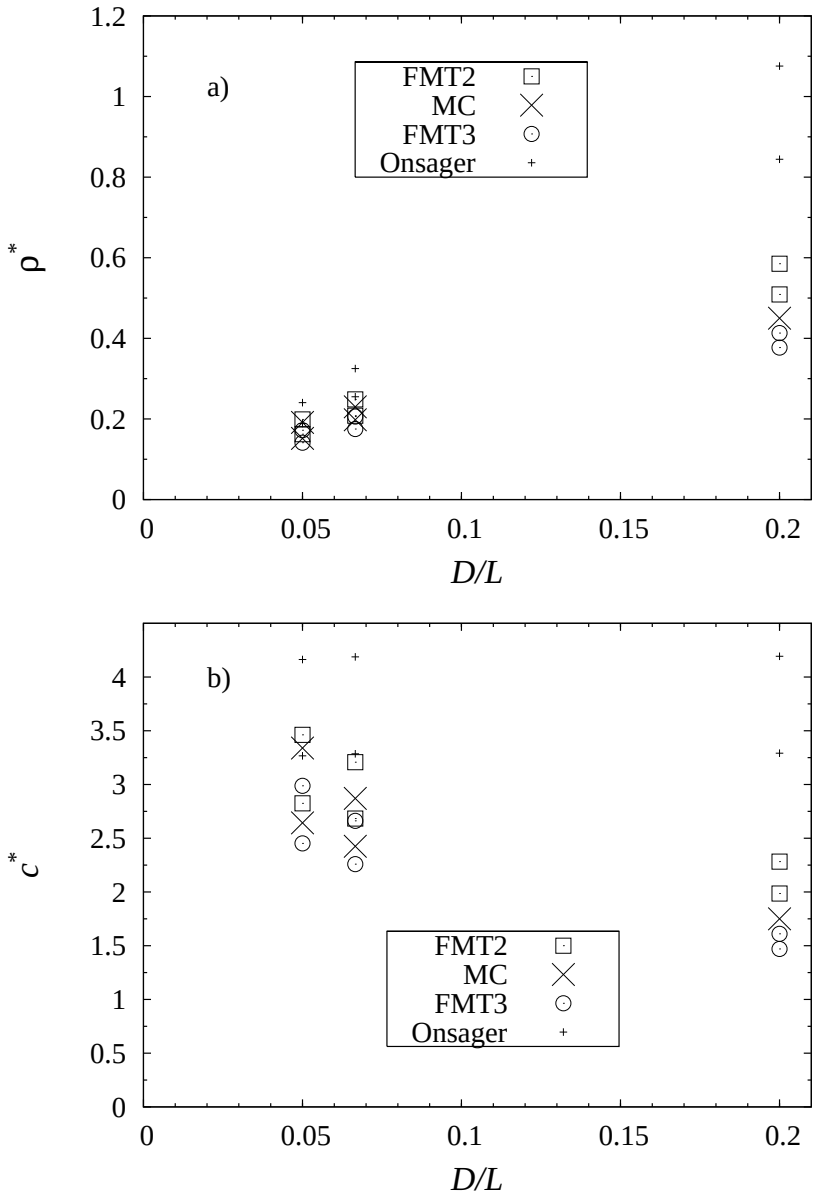

Figure 6.5: a) Predictions for the reduced coexistence densities ρ^* as a function of D/L. Plotted are results from Onsager, FMT2, FMT3 and MC simulations [102], see the key for the symbols. The lower symbols denote in each case the isotropic coexistence density, the upper symbols the nematic coexistence density, respectively. For $D/L = 0.2$ no IN transition is found by MC simulations [102]. b) Same as a), but for the scaled coexistence densities c^*.

Chapter 7

Summary and Outlook

In conclusion, we have investigated hard colloidal platelets in bulk and in external fields with FMT. This FMT functional includes contributions to the free energy that are of third order in density. For reasons of comparison, we performed additional calculations for hard rods. We initially treated bulk systems and find our FMT functional to describe the IN transition and the equation of state very well compared to MC simulation results (performed by M.Dijkstra, [115]). Next we have investigated the free IN interface and the behaviour of platelets adsorbed against a single hard wall. For the free IN interface we find the decay on the isotropic as well as on the nematic side to be monotonic, which is in contrast to predictions from Onsager theory [115]. FMT also predicts complete wetting of the wall by the nematic phase, which was confirmed by the MC simulations. Surprisingly, we find oscillations of the wall density profile for small (bulk) densities which disappear with increasing (bulk) density. This seems to be confirmed by the MC simulations, but a final statement is not yet possible due to the strong thermal fluctuations of the profiles obtained in the simulations.

Subsequently we have turned to finite external fields and treated platelets supposed to a magnetic field, gravity and a simultaneous presence of both. For a magnetic field, we find the density and order parameter jump at the IN transition to become smaller and finally to end in a critical point for strong magnetic fields. The simultaneous magnetic and gravitational field was treated with a LDA approach and the full z-dependent FMT functional. While the latter contains nonlocal correlations, these are not present in the LDA approach. Consistently from both approaches we find a reduction of density at the bottom of the system when increasing the field strength. Oscillations of the density profile at the upper wall found with the z-dependent FMT are not catched by the LDA approach as can be expected from its local

nature which yields monotonic results. We have also computed the product of the density profile with the order parameter, which is of experimental interest and thus could allow tests of our results, see below. Afterwards, we have investigated platelets in strong geometric confinement induced by two parallel planar hard walls and find a capillary critical capillary width upon decreasing the wall distance. For smaller distances no first order IN transition is found. We compare our findings with a calculation of capillary nematization of hard rods and find a remarkable larger critical capillary width for platelets. We explain this with the correlation lengths at the isotropic and nematic side of the free IN interface ξ_I and ξ_N, which are larger for platelets. In the last chapter we have tested an extension of FMT to describe thick platelets and rods. We have computed the dependence of the IN transition on the thickness of the particles. We find that the predictions of the extended FMT for rods are in better agreement with the simulation results than for platelets and can be compared with those of a different approach [51]. Nevertheless we have to conclude that the results are not satisfying for both platelets and rods.

Possible future work could be devoted to answering the question of the disappearance of the oscillations of the wall profile with increasing density. This could be done by longer runs with MC simulations to reduce thermal noise as well as with FMT calculations with larger z and θ resolution. A connection to experiments could be done for our predictions of the sedimentation profiles, especially the product of the density profile and that of the order parameter: the retardation of light sent through a test tube with colloidal particles is proportional to this product and can be measured experimentally [66]. From our investigation of platelets and rods with finite thickness, we have to conclude that a more profound modification of the FMT than performed in this work is necessary to obtain quantitatively accurate results.

Bibliography

[1] L. Tonks, Phys. Rev. **50**, 955 (1936).

[2] see, e. g, S. M. Oversteegen, and R. Roth, J. Chem. Phys. **122**, 214502 (2005).

[3] H. Zocher, Z. Anorg. Chem. **147**, 91 (1925).

[4] F. C. Bawden, N. W. Pirie, J. D. Bernal, and I. Fankuchen, Nature **138**, 1051 (1936).

[5] L. Onsager, Ann. (N.Y.) Acad. Sci. **51**, 627 (1949).

[6] D. Frenkel and R. Eppenga, Phys. Rev. Lett. **49**, 1089 (1982).

[7] M. Bates and D. Frenkel, Phys. Rev. E **57**, 4824 (1998).

[8] F. M. van der Kooij, K. Kassapidou, and H. N. W. Lekkerkerker, J. Phys. Chem. B. **102**, 7829 (1998).

[9] F. M. van der Kooij, K. Kassapidou, and H. N. W. Lekkerkerker, Nature **406**, 868 (2000).

[10] D. van der Beek, A. V. Petukhov, S. M. Oversteegen, G. J. Vroege, and H. N. W. Lekkerkerker, Euro. Phys. J. E. **16**, 253 (2005).

[11] D. van der Beek and H. N. W. Lekkerkerker, Europhys. Lett. **61**, 702 (2003).

[12] D. van der Beek and H. N. W. Lekkerkerker, Langmuir **20**, 8582 (2004).

[13] J. E. G. J. Wijnhoven, D. D. van 't Zand, D. van der Beek, and H. N. W. Lekkerkerker, Langmuir **21**, 10422 (2005).

[14] D. van der Beek, T. Schilling, and H. N. W. Lekkerkerker, J. Chem. Phys. **121**, 5423 (2004).

[15] D. van der Beek, A. V. Petukhov, P. Davidson, J. Ferre, J. P. Jamet, H. H. Wensink, G. J. Vroege, W. Bras, and H. N. W. Lekkerkerker, Phys. Rev. E **73**, 041402 (2006).

[16] Z. X. Zhang and J. S. van Duijneveldt, J. Chem. Phys. **124**, 154910 (2006).

[17] C. Pizzey, J. S. van Duijneveldt, and S. Klein, Mol. Cryst. and Liquid Cryst. **409**, 51 (2004).

[18] S. D. Zhang, P. A. Reynolds, and J. S. van Duijneveldt, J. Chem. Phys. **117**, 9947 (2002).

[19] S. D. Zhang, P. A. Reynolds, and J. S. van Duijneveldt, Mol. Phys. **100**, 3041 (2002).

[20] H. H. Wensink and H. N. W. Lekkerkerker, Europhys. Lett. **66**, 125 (2004).

[21] H. H. Wensink, G. J. Vroege, and H. N. W. Lekkerkerker, J. Phys. Chem. B. **105**, 10610 (2001).

[22] S. M. Oversteegen and H. N. W. Lekkerkerker, J. Chem. Phys. **120**, 2470 (2004).

[23] M. Bier, L. Harnau, and S. Dietrich, J. Chem. Phys. **123**, 114906 (2005).

[24] Y. Martinez-Raton and J. A. Cuesta, Phys. Rev. Lett. **89**, 185701 (2002).

[25] A. Poniewierski, Phys. Rev. E **47**, 3396 (1993).

[26] R. van Roij, M. Dijkstra, and R. Evans, Europhys. Lett. **49**, 350 (2000).

[27] R. van Roij, M. Dijkstra, and R. Evans, J. Chem. Phys. **113**, 7689 (2000).

[28] M. Dijkstra, R. van Roij, and R. Evans, Phys. Rev. E **63**, 051703 (2001).

[29] M. Schmidt, H. Löwen, J. M. Brader, and R. Evans, J. Phys.: Condensed Matter **14**, 9353 (2002).

[30] R. Roth, J. M. Brader, and M. Schmidt, Europhys. Lett. **63**, 549 (2003).

[31] J. M. Brader, R. Evans, and M. Schmidt, Mol. Phys. **101**, 3349 (2003).

[32] R. Evans, J. M. Brader, R. Roth, M. Dijkstra, M. Schmidt, and H. Löwen, Phil. Trans. Roy. Soc. A **359**, 961 (2001).

[33] M. Dijkstra and R. van Roij, Phys. Rev. Lett. **89**, 208303 (2002).

[34] M. Dijkstra, R. van Roij, R. Roth, and A. Fortini, Phys. Rev. E **73**, 041404 (2006).

[35] L. Harnau and S. Dietrich, Phys. Rev. E **65**, 021505 (2002).

[36] L. Harnau and S. Dietrich, Phys. Rev. E **66**, 051702 (2002).

[37] M. Bier, L. Harnau, and S. Dietrich, Phys. Rev. E **69**, 021506 (2004).

[38] A. Esztermann, H. Reich, and M. Schmidt, Phys. Rev. E **73**, 011409 (2006).

[39] R. Evans, in *Fundamentals of Inhomogeneous Fluids*, edited by D. Henderson (Dekker, New York, 1992), Chap. 3, p. 85.

[40] P. Hohenberg and W. Kohn, Phys. Rev. B **136**, B864 (1964).

[41] W. Kohn and L. J. Sham, Phys. Rev. **140**, A1133 (1965).

[42] N. D. Mermin, Phys. Rev. **137**, A1141 (1965).

[43] L. Harnau, D. Costa, and J. P. Hansen, Europhys. Lett. **53**, 729 (2001).

[44] Y. Martinez-Raton and J. A. Cuesta, J. Chem. Phys. **111**, 317 (1999).

[45] Y. Martinez-Raton and J. A. Cuesta, J. Chem. Phys. **118**, 10164 (2003).

[46] Y. Martinez-Raton, Phys. Rev. E **69**, 061712 (2004).

[47] Y. Martinez-Raton, E. Velasco, and L. Mederos, J. Chem. Phys. **125**, 014501 (2006).

[48] Y. Rosenfeld, Phys. Rev. Lett. **63**, 980 (1989).

[49] Y. Rosenfeld, Phys. Rev. E **50**, R3318 (1994).

[50] Y. Rosenfeld, Mol. Phys. **86**, 637 (1995).

[51] G. Cinacchi and F. Schmid, J. Phys.: Condensed Matter **14**, 12223 (2002).

[52] P. Tarazona and Y. Rosenfeld, Phys. Rev. E **55**, R4873 (1997).

[53] J. A. Cuesta, Y. Martinez-Raton, and P. Tarazona, J. Phys.: Condensed Matter **14**, 11965 (2002).

[54] J. M. Brader, A. Esztermann, and M. Schmidt, Phys. Rev. E **66**, 031401 (2002).

[55] R. Ohnesorge, *Dichtestruktur und Schmelzen von Kristallen und ihren Oberflächen* (PHD thesis University München, München, 1994).

[56] R. Ohnesorge, H. Löwen, and H. Wagner, Europhys. Lett. **22**, 245 (1993).

[57] R. Ohnesorge, H. Löwen, and H. Wagner, Phys. Rev. E **50**, 4801 (1994).

[58] D. van der Beek, H. Reich, P. van der Schoot, M. Dijkstra, T. Schilling, R. Vink, M. Schmidt, R. van Roij, and H. N. W. Lekkerkerker, Phys. Rev. Lett. **97**, 087801 (2006).

[59] R. Eppenga and D. Frenkel, Mol. Phys. **2**, 1303 (1984).

[60] M. Dijkstra, J. P. Hansen, and P. A. Madden, Phys. Rev. E **55**, 3044 (1997).

[61] M. Heni and H. Löwen, Phys. Rev. E **60**, 7057 (1999).

[62] A. Fortini, M. Dijkstra, M. Schmidt, and P. P. F. Wessels, Phys. Rev. E **71**, 051403 (2005).

[63] N. Akino, F. Schmid, and M. P. Allen, Phys. Rev. E **63**, 041706 (2001).

[64] S. Wolfsheimer, C. Tanase, K. Shundyak, R. van Roij, and T. Schilling, Phys. Rev. E **73**, 061703 (2006).

[65] K. Shundyak and R. van Roij, Europhys. Lett. **74**, 1039 (2006).

[66] D. van der Beek, Private communications .

[67] J. Kerr, Phil. Mag. **50**, 337 (1875).

[68] D. van der Beek, *Liquid crystal phase behaviour of colloidal platelets in external fields* (PHD thesis Utrecht University, Utrecht, 2005).

[69] B. J. Lemaire, P. Davidson, J. Ferre, J. P. Jamet, D. Petermann, P. Panine, I. Dozov, and J. P. Jolivet, Eur. Phys. J. E **13**, 291 (2004).

[70] B. J. Lemaire, P. Davidson, D. Petermann, P. Panine, I. Dozov, D. Stoenescu, and J. P. Jolivet, Eur. Phys. J. E **13**, 309 (2004).

[71] H. Nakamura and K. Okano, Phys. Rev. Lett. **50**, 186 (1983).

[72] J. Torbet and G. Maret, Biopolymers **20**, 2657 (1981).

[73] R. M. Goldstein and M. W. Mueller, Phys. Rev. B Solid State **2**, 4585 (1970).

[74] Y. Watanabe, A. Nakano, and A. Sato, Material Science and Engineering A **146**, 151 (1991).

[75] A. R. Khoklov and A. N. Semenov, Macromolecules **15**, 1272 (1982).

[76] S. Varga, G. Jackson, and I. Szalai, Mol. Phys. **93**, 377 (1998).

[77] J. D. Parsons, Phys. Rev. A **19**, 1225 (1979).

[78] S. D. Lee, J. Chem. Phys. **87**, 4972 (1987).

[79] S. D. Lee, J. Chem. Phys. **89**, 7036 (1988).

[80] H. Graf and H. Löwen, J. Phys.: Condensed Matter **11**, 1435 (1999).

[81] S. Varga, G. Kronome, and I. Szalai, Mol. Phys. **98**, 911 (2000).

[82] J. Perrin, J. Physique **9**, 5 (1910).

[83] T. Biben, J. P. Hansen, and J. L. Barrat, J. Chem. Phys. **98**, 7330 (1993).

[84] R. Piazza, T. Bellini, and V. Degiorgio, Phys. Rev. Lett. **71**, 4267 (1993).

[85] D. van der Beek, T. Schilling, and H. N. W. Lekkerkerker, J. Chem. Phys. **121**, 5423 (2004).

[86] M. Schmidt, M. Dijkstra, and J. P. Hansen, J. Phys.: Condensed Matter **16**, 4185 (2004).

[87] M. Schmidt, M. Dijkstra, and J. P. Hansen, Phys. Rev. Lett. **93**, 088303 (2004).

[88] A. Esztermann and H. Löwen, Europhys. Lett. **68**, 120 (2004).

[89] V. M. Buzmakov, Coll. J. **57**, 11 (1995).

[90] C. Galindo-Gonzalez, J. de Vicente, M. M. Ramos-Tejada, M. T. Lopez-Lopez, F. Gonzalez-Caballero, and J. D. G. Duran, Langmuir **21**, 4410 (2005).

[91] R. Evans and U. M. B. Marconi, J. Chem. Phys. **86**, 7138 (1987).

[92] R. Evans, J. Phys.: Condensed Matter **2**, 8989 (1990).

[93] P. Sheng, Phys. Rev. A **26**, 1610 (1982).

[94] M. M. T. da Gama and P. Tarazona, Phys. Rev. A **41**, 1149 (1990).

[95] Y. Mao, P. Bladon, H. N. W. Lekkerkerker, and M. E. Cates, Mol. Phys. **92**, 151 (1997).

[96] D. L. Cheung and F. Schmid, J. Chem. Phys. **120**, 19 (2004).

[97] M. Lagomarsino, M. Dogterom, and M. Dijkstra, J. Chem. Phys. **119**, 6 (2003).

[98] D. de las Heras, E. Velasco, and L. Mederos, J. Chem. Phys. **120**, 10 (2004).

[99] D. de las Heras, E. Velasco, and L. Mederos, Phys. Rev. Lett. **94**, 017801 (2005).

[100] M. M. T. da Gama, P. Tarazona, M. P. Allen, and R. Evans, Mol. Phys. **71**, 801 (1990).

[101] K. Shundyak, *Interfacial phenomena in hard rod fluids* (PHD thesis Utrecht University, Utrecht, 2004).

[102] P. Bolhuis and D. Frenkel, J. Chem. Phys. **106**, 666 (1997).

[103] M. A. Cotter and D. E. Martire, J. Chem. Phys. **52**, 1902 (1970).

[104] S. C. McGrother, D. C. Williamson, and G. Jackson, J. Chem. Phys. **104**, 6755 (1996).

[105] P. J. Camp, C. P. Mason, M. P. Allen, A. A. Khare, and D. A. Kofke, J. Chem. Phys. **105**, 2837 (1996).

[106] A. Poniewierski and R. Holyst, Phys. Rev. Lett. **61**, 2461 (1988).

[107] R. Holyst and A. Poliewierski, Phys. Rev. A **39**, 2742 (1989).

[108] R. Holyst and A. Poliewierski, Mol. Phys. **68**, 381 (1990).

[109] R. Holyst and A. Poliewierski, Phys. Rev. A **41**, 6871 (1990).

[110] A. M. Somoza and P. Tarazona, Phys. Rev. Lett. **61**, 2566 (1988).

[111] A. M. Somoza and P. Tarazona, J. Chem. Phys. **91**, 517 (1989).

[112] A. M. Somoza and P. Tarazona, Phys. Rev. A **41**, 965 (1990).

[113] G. Cinacchi, Y. Martinez-Raton, L. Mederos, and E. Velasco, J. Chem. Phys. **124**, 234904 (2006).

[114] F. R. Ree and W. G. Hoover, J. Chem. Phys. **40**, 939 (1964).

[115] H. Reich, M. Dijkstra, R. van Roij, and M. Schmidt, to be published .

Acknowledgments

First of all I thank Matthias Schmidt for his immense support. Without his assistance and ideas this thesis could not have been finished.

I also thank Hartmut Löwen for the opportunity to work at this institute.

All members of the institute I thank for the good working atmosphere.

I thank the SFB-TR6 for the financial support.

I thank Rene v. Roij (Utrecht University) and M. Dijkstra (also Utrecht University) for the permission to use their results (Onsager theory calculations and MC simulations, respectively) in this thesis.

Most of all, I thank my parents for all their love and manifold support.

Die hier vorgelegte Dissertation habe ich eigenständig und ohne unerlaubte Hilfe angefertigt. Die Dissertation wurde in der vorgelegten oder in ähnlicher Form noch bei keiner anderen Institution eingereicht. Ich habe bisher keine erfolglosen Promotionsversuche unternommen.

Düsseldorf, den 10.12.2006

(Hendrik Reich)